uOttawa

L'Université canadienne
Canada's university

FACULTÉ DES ÉTUDES SUPÉRIEURES
ET POSTOCTORALES

uOttawa

L'Université canadienne
Canada's university

FACULTY OF GRADUATE AND
POSDOCTORAL STUDIES

Alain R. Gauthier
AUTEUR DE LA THÈSE / AUTHOR OF THESIS

M.Sc. (Physics)
GRADE / DEGREE

Department of Physics
FACULTÉ, ÉCOLE, DÉPARTEMENT / FACULTY, SCHOOL, DEPARTMENT

The Permeability of a Lipid Bilayer
TITRE DE LA THÈSE / TITLE OF THESIS

B. Joós
DIRECTEUR (DIRECTRICE) DE LA THÈSE / THESIS SUPERVISOR

CO-DIRECTEUR (CO-DIRECTRICE) DE LA THÈSE / THESIS CO-SUPERVISOR

EXAMINATEURS (EXAMINATRICES) DE LA THÈSE / THESIS EXAMINERS

H. Logan

M. Kaern

R. Taylor

Gary W. Slater
LE DOYEN DE LA FACULTÉ DES ÉTUDES SUPÉRIEURES ET POSTDOCTORALES /
DEAN OF THE FACULTY OF GRADUATE AND POSTDOCORAL STUDIES

The Permeability of a Lipid Bilayer

by

Alain R. Gauthier

Thesis submitted to the
Faculty of Graduate and Postdoctoral Studies
In partial fulfillment of the requirements
For the Master of Science in Physics

Department of Physics
Faculty of Science
University of Ottawa

Library and
Archives Canada

Published Heritage
Branch

395 Wellington Street
Ottawa ON K1A 0N4
Canada

Bibliothèque et
Archives Canada

Direction du
Patrimoine de l'édition

395, rue Wellington
Ottawa ON K1A 0N4
Canada

Your file Votre référence
ISBN: 978-0-494-14909-6
Our file Notre référence
ISBN: 978-0-494-14909-6

NOTICE:
The author has granted a non-exclusive license allowing Library and Archives Canada to reproduce, publish, archive, preserve, conserve, communicate to the public by telecommunication or on the Internet, loan, distribute and sell theses worldwide, for commercial or non-commercial purposes, in microform, paper, electronic and/or any other formats.

The author retains copyright ownership and moral rights in this thesis. Neither the thesis nor substantial extracts from it may be printed or otherwise reproduced without the author's permission.

AVIS:
L'auteur a accordé une licence non exclusive permettant à la Bibliothèque et Archives Canada de reproduire, publier, archiver, sauvegarder, conserver, transmettre au public par télécommunication ou par l'Internet, prêter, distribuer et vendre des thèses partout dans le monde, à des fins commerciales ou autres, sur support microforme, papier, électronique et/ou autres formats.

L'auteur conserve la propriété du droit d'auteur et des droits moraux qui protège cette thèse. Ni la thèse ni des extraits substantiels de celle-ci ne doivent être imprimés ou autrement reproduits sans son autorisation.

In compliance with the Canadian Privacy Act some supporting forms may have been removed from this thesis.

While these forms may be included in the document page count, their removal does not represent any loss of content from the thesis.

Conformément à la loi canadienne sur la protection de la vie privée, quelques formulaires secondaires ont été enlevés de cette thèse.

Bien que ces formulaires aient inclus dans la pagination, il n'y aura aucun contenu manquant.

Canada

Abstract

This work presents results on the permeability of a lipid bilayer to water molecules. We look at the change in bilayer permeability as a function of lipid structure and area per lipid molecule. A molecular dynamic simulation (MDS) of a solvent surfactant system was used in the canonical ensemble to simulate the membranes. Permeability was obtained by calculating the permeative resistance. This method, developed by Marrink and Berendsen, allows the sampling of very long time scale events on short time scale simulations. The structural properties of the simulated bilayer are studied and compared both to atomistic MDS and experiments. The elasticity of the simulated membranes are shown to be in good agreement with experimental results. The permeation is found to increase only slightly for a relative stretch of up to 20%, a result which is qualitatively similar to recent experiments. The increase is described by a linear relation between the permeability and the relative extension. Most of the changes in the lipid bilayer are found to occur in the central part near the ends of the tails. The effect of lipid packing on bilayer permeability are also discussed.

Acknowledgements

I would first like to thank my supervisor Dr. Béla Joós for giving me the opportunity to pursue graduate studies. His guidance and passion for science has served as a source of inspiration throughout my M.Sc. program. I would also like to thank Matthew Wallace who has given me elements of the source code used to generate the data presented in this thesis and an excellent formatting tool with which this thesis was written. I thank my friends and family who have been there for me over the course of the last two years. Foremost, I would like to thank my mother who has supported and encouraged me throughout my studies.

Contents

List of Figures

List of Tables

Chapter 1 Introduction

The cell is an incredible molecular machine and the foundation of all life. Its interior is separated from the surrounding environment by a thin oily membrane as was shown by the pioneering work of Pfeffer [1]. A typical animal cell membrane is composed of proteins and cholesterol all of which are dissolved into a lipid bilayer. The bilayer acts as a solvent for the various elements of the plasma membranes. Proteins such as actin give cells structural strength whereas other proteins such as aquaporin function as active transport gates for water molecules. In the presence of on osmotic gradient, a cell will absorb or release water from its interior into the environment until an equilibrium is reached. A majority of the water released is through by diffusion through the lipid bilayer. Transport across the lipid bilayer is a type of passive transport which accounts for the permeability of most hydrophobic molecules such as O_2, N_2 and small uncharged polar molecular groups like water and urea [1]. A majority of the small molecules that flow through the lipid bilayer either diffuses directly through the membrane interior or through small hydrophobic pores induced by thermal fluctuations [2].

The transport properties of lipid membranes have been studied now for over 100 years. The first studies pioneered by Overton found that the rate at which a substance crossed cell membranes was strongly correlated with its solubility in oil [3]. Initial studies of the permeability of biological membranes focused on understanding the potency of certain anesthetics. Since then, the study of membrane transport has exploded into branches of biology, physiology, biochemistry, chemistry, and physics unearthing many pressing questions. From a physicist's point of view, cell membranes offer a wealth of intriguing problems. In this thesis, the transport properties of lipid bilayers will be examined. The following sections will introduce the reader to some of the basic properties of lipids and lipid bilayers. This will be followed by a more complete statement of the objectives of this thesis.

1.1 Lipids and the Lipid Bilayer

The lipid is a general category of chemical molecules characterized by one fatty acid chain, or two, and a polar head group. There exist three different types of lipids: triglycerides, steroids and phospholipids which are classified by the composition of the head groups and tail groups. Triglycerides consist of a glycerol group esterified with three fatty acid chains. These lipids are stored in fat cells, and later broken down when the body demands fatty acids [4]. Lipids in the steroid group are characterized by a small polar head attached to four fused rings, the steriod rings [4] and a short nonpolar hydrocarbon tail. The most important group of lipid in this family is cholesterol which is very abundant in eucaryotic cell membranes [1].

The most abundant type of lipid in the plasma membrane is the phospholipid [1]. It is characterized by the presence of a phosphate group in the head section. A typical phospholipid is Dimyristoylphosphatidylcholine (DMPC) which is shown in figure 3.1. The head section of this molecule is subdivided into a choline group, a phosphate group, and a glycerol group as well as a tail section composed of two fatty acid chains. The polarity of the head section originates from the positive charge in the choline group and the negative charge on the phosphate group. On its own, the head of the lipid would be soluble in water so it is said to be hydrophilic. At the bottom of the head section is the glycerol group which is linked to the tails by an ester linkage ($R' - COO - R'$) as shown in Fig. 3.1. The head group is much shorter then the tail section and makes up about a quarter of the lipids length.

The non polar tail section is composed of two fatty acids called myristic acid which are $14 - 24$ carbon atoms long. The tail section is flexible, whereas the head section is not. Double bonds can form along one of the tails of the lipid which leaves this tail unsaturated. These bonds have an interaction energy of $240 k_B T_{Room}$, where k_B is Boltzmann's constant and T_{Room} is room temperature, which makes them more

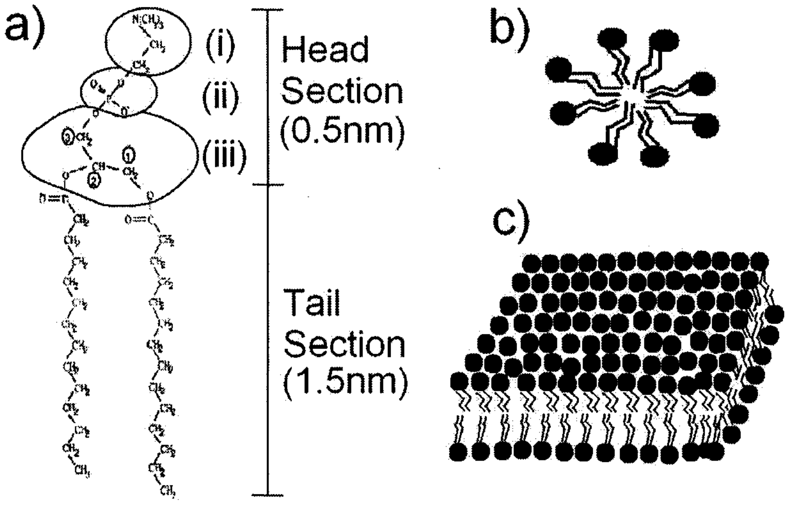

Figure 1.1: a) The chemical structure of a lipid (adapted from reference [5]) where the head section is composed of (i) choline, (ii) phosphate, and (iii) glycerol groups. The tail section, made of fatty acid chains, is bonded to the glycerol group and is hydrophobic. When lipids are placed in an aqueous environment, structures such as b) micelles and c) bilayers self-assemble.

rigid then the single bond, whose interaction energy is $140k_BT_{Room}$. Double bonds form kinks along the tail and reduces its flexibility, influencing the ability of the lipids to pack against each other [5]. Because the head section is hydrophilic, and the tail section is hydrophobic, the phospholipid is known as an amphiphilic molecule whose behavior is of great interest when placed in water.

1.2 Hydrophobic Effect

The charge within a water molecule is not uniformly distributed due to the difference in electronegativity between the hydrogen and oxygen atoms. The electronegativity of O ($\sim$ 3.5 on the Pauling scale) is higher then that of H ($\sim$ 2.1 on the Pauling scale) which leaves the oxygen atom slightly negative, and the hydrogen atoms slightly positive. This difference in charge induces a bond between water molecules, known as the hydrogen bond. At room temperature, hydrogen bonding causes the formation of complex unordered networks in bulk water. These bonds decrease the energy of the system at the expense of limiting the number of configurations available to the system, hence decreasing the entropy. These two effects combine in such a way that the Helmholtz free energy defined as,

$$F = E - TS, \tag{1.1}$$

is minimized. When a non polar molecule is introduced into bulk water, space must be made in order to accommodate its presence within the liquid. Either the water molecules adjacent to the lipid tails undo their H-bonds, raising the local system energy, or the H_2O molecules form hydrogen bonded cages, or a clathrate cage, around the intruder thus decreasing the local entropy [5]. It is clear from Eq. (1.1) that both of these responses will cause the free energy to increase. Therefore, in a water lipid mixture, the system will have a tendency to minimize the exposer of the tail sections to water molecules. This effect is known as the hydrophobic effect and is the driving force behind membrane self assembly.

The amphiphilic nature of the lipids gives rise to intriguing properties when placed in an aqueous environment at appropriate concentrations. Because the tails of the lipids are hydrophobic and their heads are hydrophilic, lipids will tend to orient themselves with their head sections pointing outwards towards the water phase and tails pointing inward, bunched together. Depending on the concentration of lipids in solution, various structures can be obtained. Two such structures are the spherical micelle and the bilayer (see figure 3.1). The spherical micelles will first appear at the critical micelle concentration [6]. As the lipid concentration grows, micelles become less energetically favorable and may join together into tubular structures. Further increases of lipid concentration will lead to the development of mirrored sheets of lipids, or bilayers. Just as micelles, bilayers will self-assemble in a water solution if the lipid concentration is just right.

1.3 Lipid Movement Within the Bilayer and Phase Transitions

Lipids typically undergo three types of movements in the bilayer matrix: rotations about its own axis, lateral diffusion within a monolayer and a "flip-flop" from one monolayer to the other. A number of experimental studies on vesicles and artificial membrane have shown that "flip-flop" events are quite rare [1]. The long time between "flip-flop" events is not surprising since the head particle must traverse the tail section and overcome a huge energy barrier in order to reach the other side [7]. When "flip-flop" events do occur, they do so on a very short time interval on the order of a few tens of picoseconds [8]. The lipids within a monolayer undergo both rotational and translational motion. The lateral diffusion coefficient, D_{lat}, describes the two dimensional translational motion of the lipid within the monolayer. This quantity is easily obtained from simulation from the slope of a plot of the mean squared displacement as a function of time:

$$D = \lim_{t \to \infty} \frac{\langle [r_{CM}(t) - r_{CM}(0)]^2 \rangle}{2dt} \tag{1.2}$$

where d is the dimension, $d = 2$ in the case of a bilayer, and $r_{CM}(t)$ is the displacement relative to the center of mass of the system. Experimental data of the diffusion coefficient obtained from NMR spectra have shown that D_{lat} is about $5\mu m^2/s$ [9]. The rotation of a lipid about its own axis is much faster, occurring on a much shorter time scale on the order of $10^{-10} - 10^{-9}s$, several orders of magnitude faster then the translational motion. The lateral diffusion is sensitive to a number of bilayer properties. It depends for instance exponentially on the hydration of the bilayer [6, 10], and has been found to decrease with increasing cholesterol content [7]. Both the hydration level (number of water particles per lipid) and cholesterol affect the way in which lipids pack together, and how they slide against one another. Temperature is also a critical factor of the lateral diffusion of the lipids in a monolayer.

Depending on the temperature, the lipid bilayer may be in a one of many different phases. Figure 1.2 shows the $n_w - T$ phase diagram where n_w is the percentage of water hydration and T is the temperature. As the membrane cools or dehydrates, the

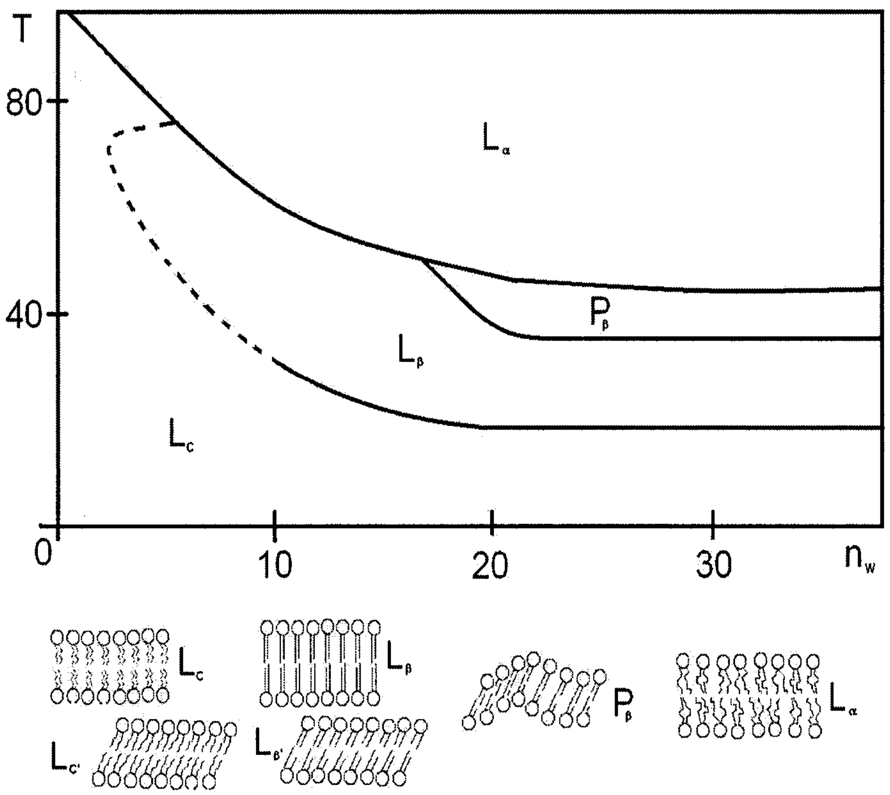

Figure 1.2: T-n_w phase diagram for DPPC lipids. Cartoon representation of four different bilayer states (adapted from [6])

lipids pack together producing the different phases. Each phase has a characteristic ordering of the tails which can be studied using the $2d$ radial distribution function $g_{xy}(r)$. The unormalized $g_{xy}(r)$ is defined as:

$$g_{xy}(r) = \frac{2A}{N^2}\left\langle \sum_{i=1}^{N}\sum_{j=i}^{N}\delta(\mathbf{r} - [\mathbf{r}_i - \mathbf{r}_j]) \right\rangle \tag{1.3}$$

where N is the number of lipids in a monolayer, A is the total area of the surface and the brackets denote an ensemble average. The RDF gives the total number of lipids within a disc of radius r and thickness δr centered on lipid i [11, 9]. Therefore, $g_{xy}(r)$ describes how pairs of lipids are distributed as a function of the distance which separates them. This quantity is easily obtained from simulation and can be compared with experimental data collected using diffraction patterns. The crystalline phase L_C or $L_{C'}$ is the most common at very low hydration. In this phase, the lipids are arranged in a crystal-like structure and pack tightly together so that the bilayer displays long range order in the lateral direction. As the temperature rises, there is a subtransition to the gel state, L_β or $L_{\beta'}$. Compared to the crystalline phase, there is a slight increase in the area per lipid due to an increase in the rotation of the lipid about its own axis. The lipids are less tightly packed together and the ordering within a monolayer extends only up to a few nearest neighbors [9]. Depending on the hydration of the head groups, there may be a second subtransition from the gel phase to the ripple phase. The ripple phase, $P_{\beta'}$ is an intermediary between the gel and liquid crystalline phases found only in certain lipids. In this phase the lipids are packed together in such a way that the bilayer surface is rippled.

Further increases in temperature lead to the chain melting transition and the appearance of a liquid crystal phase. In the liquid crystalline phase the lipids behave as a two dimensional liquid, diffusing freely within each of the monolayers. Computer simulations have shown that the D_{lat} is much larger in the liquid phase than in the other phases [9]. The transition from gel to liquid crystalline is first order during which the ordering of the lipid tails is lost and a substantial increase in the lateral diffusion coefficient is observed. The liquid to gel transition is of great importance to biological processes because it occurs in temperature ranges relevant to biological functions. It is most typically characterized by a discontinuity in the area per lipid versus temperature graph, as reported by computer simulations. A peak in the heat capacity is also observed during this phase transition [12, 10, 6]. Because of its sensitivity to the packing of the lipids the amount of cholesterol, water content, number of double bonds per lipid chain and number CH_2 groups in the tails will all influence the liquid to gel transition temperature [13, 14, 15, 9, 6].

1.4 The Thesis Topic: Permeability and Membrane Extension

Transport across the lipid bilayer is a type of passive transport which accounts for the permeability of most hydrophobic molecules such as O_2, N_2 and small uncharged polar molecular groups like water and urea [1]. A majority of the small molecules that flow through the lipid bilayer either diffuses directly through the membrane interior or through small hydrophobic pores induced by thermal fluctuations [2].

In a previous study, the Joós group looked at the rupture of lipid bilayers [17]. The degree of water permeation is crucial in understanding the nucleation energy for the formation of pores. The previous work of our group showed that these transient pores combine together and ultimately lead to the rupture of the membrane. This work approaches the issue of the response of the membrane to stress before pore formation, as we are trying to understand the changes in resistance to water penetration as the area per lipid increases.

The main questions we will try to answer in this thesis are: *How does the permeability of water across a lipid bilayer change as the membrane is stretched. How is the structure of the bilayer affected by the increased area per lipid?*

To address these questions, simulations of the membrane are carried out on the length scale of several nanometers and a time scale of nanoseconds. The membrane is studied using a molecular dynamics simulation (MDS) of a solvent surfactant system. A MDS methodology was chosen to understand the molecular origins of permeability and stretching effects on the membrane, thus limiting the need for assumptions on the nature of the transport process. The permeability is then obtained indirectly by calculating the resistance of the membrane to water flow. In chapter 2, some theoretical models of the permeability of lipid membranes and an overview of some experimental results is presented. In chapters 3, I present the MDS model used to simulate the lipid bilayer while in chapter 4 some results on the elasticity of the lipid bilayer are presented. Chapter 5 will overview the techniques used to obtain the permeability and compare our findings with those of several other groups. The effects of coarse graining will also be discussed. In chapters 6, the stretching effects on bilayer structure and permeability are shown.

Chapter 2 Permeability: Models and Background

Passive transport across a bilayer depends both on the characteristics of the solute and those of the membrane. This chapter describes the diffusive flow of water across a bilayer lipid membrane (BLM). The permeability of a membrane relates the flow, J to a driving force. Making no assumptions about the nature of the permeant, then the possible driving forces are the difference in concentration of solutes on either side of the BLM (Δc_s), the difference in hydrostatic pressure (Δp), the electric field in the case of charged species (E) and to a lesser extent the temperature gradient [18]. In the early 60's, Kedem and Katchalsky derived phenomenological equations which describe the flow across a membrane in terms of the first three of the aforementioned forces [19]. These equations, derived within the framework of the nonequilibrium thermodynamics, are:

$$\begin{aligned} J_v &= L_{11}(\Delta p - \Delta\Pi) + L_{12}(\Delta\Pi_s - c_s) + L_{13}E \\ J_s &= L_{21}(\Delta p - \Delta\Pi) + L_{22}(\Delta\Pi_s/c_s) + L_{23}E \\ I &= L_{31}(\Delta p - \Delta\Pi) + L_{32}(\Delta\Pi_s/c_s) + L_{33}E \end{aligned} \tag{2.1}$$

where J_v is the total flow, J_s is the solute flow and I is the current across the membrane. A concentration gradient of either permeable or impermeable solute will generate an osmotic pressure of $\Delta\Pi = RT\Delta c$. In Eq. (2.1), the $\Delta\Pi_s$ represents the osmotic pressure induced by the permeable solutes and $\Delta\Pi$ is the contribution of both the permeable and impermeable solutes (assumed to be additive). The matrix L_{ij} describes the response of the membrane to an applied gradient.

Are main interest in this work is the permeability of water so that there are no permeable solute ($\Delta\Pi_s = 0, J_s = 0$) present in solution. Charge effects ($E = 0$,$I = 0$) are also neglected. An impermeable solute is present in the system which produces an osmotic gradient across the membrane. With these assumptions, Eq. (2.1) reduce to:

$$L_{11} = \left(\frac{J_v}{\Delta p - \Delta\Pi}\right)_{\Delta\Pi_s, E} \tag{2.2}$$

The quantity L_{11} defines the hydraulic permeability. In the literature, it is usually represented as L_p [2]. Other assumptions give similar expressions for the permeability of the solutes and ions. In all these cases, the permeability is defined as *"the rate of transfer of a molecular species under specified conditions"* (from [18]).

In order to write the permeability in terms of the solute properties within the membrane, assumptions need to be made about the nature of the transport process. Surprisingly, a very simple model known as the homogeneous solubility diffusion model (HSDM) does a very good job of explaining much of the transport properties of BLM. Experiments have shown that the HSDM correctly predicts the dependence of permeability on membrane thickness and on a permeant's solubility in the hydrocarbon tails. However it does not give any details about the distribution of the resistance to permeation within the membrane. A more sophisticated model, the inhomogeneous solubility diffusion model (ISDM) has done just this and allowed for the calculation of the permeability coefficient using computer simulations of BLM.

2.1 Experimental Values of Water Permeability

In table 2.1, values of the permeability of water through various lipid bilayers are presented. These values span about an order of magnitude, depending on the lipid tail length, temperature and contents of the membrane (true for the red blood cell). All measurements where done with bilayers in the liquid crystalline state.

Experimental measurements of the lipid permeability are most commonly done using the micropipette aspiration technics. In this technic, lipid vesicles, or cells, are first placed in a control solution of glucose and water. The vesicle is allowed to

Table 2.1: Permeability of water molecules across lipid bilayers.

Membrane	$P_{exp}(cm/s)$	Reference
Phosphatidylcholine ($333K$)	4×10^{-3}	[6]
Phosphatidylcholine, 14C ($303K$)	2.4×10^{-2}	[24]
Phosphatidylcholine, 24C ($303K$)	5.0×10^{-3}	[24]
Egg PC ($310K$)	3×10^{-3}	[2]
Red Blood Cell ($340K$)	8×10^{-2}	[25]

relax until the concentration inside the vesicle is at equilibrium with its environment. Once at equilibrium, the vesicle is aspirated by a specialized syringe composed of a very fine needle, a device know as a micropipette, and placed in a second solution which has a higher solute concentration than the control solution. This produces a concentration gradient across the membrane. Water then exits the interior of the vesicle in order to equilibrate the concentration on either side of the bilayer causing a decrease in the volume of the vesicle. The force exerted on the membrane by the suction of the micropipette remains unchanged. Since the membrane is elastic, the area decrease of the membrane outside the micropipette is balanced by the increase in area inside the micropipette so that the total area remains approximately constant. The rate at which the volume of the vesicle changes is related to the the flux J of water through the membrane. The change in vesicle volume is tracked with a microscope used to measure the length of membrane that is aspirated into the micropipette. The permeability is then obtained using by Eq. (2.5) [20, 21, 2]. Light scattering experiments (see [22, 3]) as well as nuclear magnetic resonance experiments (see [23]) have also been used to measure the permeability of the vesicles.

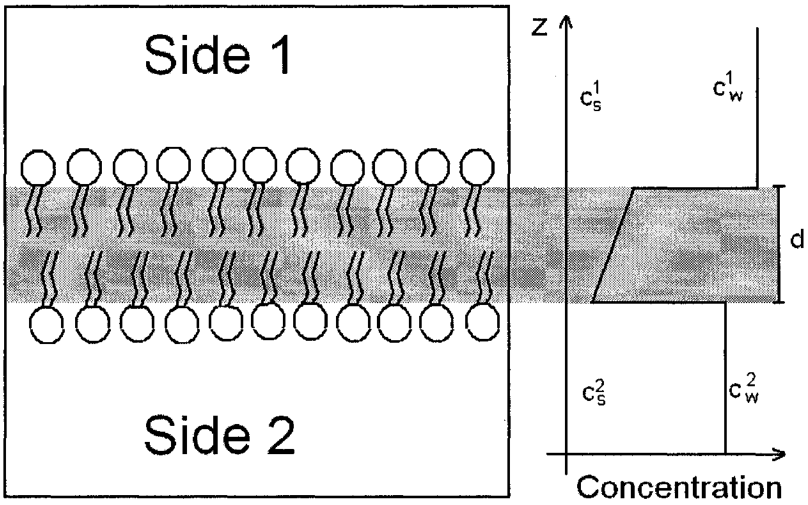

Figure 2.1: Representation of the system used to derive the HSDM. In this model, the BLM is reduced to an oil membrane (gray) of thickness d. The system consists of two solutions on either side of an oil membrane, each with its respective concentration of impermeable solute $c_s^1 < c_s^2$. This produces an osmotic pressure inducing a flow of water from side 1 to side 2. The water concentration inside the membrane is assumed to decrease linearly from side 1 to 2. (Adapted from [2])

2.2 Homogenous Solubility-Diffusion Model

As was discussed in the introduction, the first studies on membrane transport showed that the permeability of a given molecule is directly proportional to its solubility in a hydrocarbon liquid such as olive oil [3]. More recent studies [2] have shown a correlation between a molecules permeability and the product of its partition coefficient and diffusion coefficient within the membrane. This correlation is shown to hold true for 16 different solutes, where P spans five orders of magnitude. It has been shown in [24] that membrane permeability to water decreases by a factor of five with increasing hydrophobic thickness. The physical origins of these correlations can be understood in the context of the HSDM.

Consider an oil membrane which separates two compartments as shown in figure 2.1. This approximation is the starting point for the HSDM. Each compartment contains a small but different amount of impenetrable solute producing a concentration gradient across the membrane, just as described in the opening paragraphs of this chapter. The boundary between the oil and water phase is very sharp so that the permeating molecules cross the membrane in two steps, they first "jump", or dissolve, into the membrane phase and once inside, they diffuse through and out the other side. Particles do this independently, they don't "see" each other with in the membrane. With in this framework, the transport process is modelled according to Fick's first law of diffusion:

$$J = -D\left(\frac{dc}{dz}\right), \tag{2.3}$$

where J is the volume flux, and D is the diffusion coefficient inside the membrane. Note that J is positive when the movement is from a lower concentration to a higher concentration. Assuming that the concentration gradient inside the membrane changes linearly (see figure 2.1), then dc/dz inside the membrane is reduced to $\Delta c^{int}/d$. The concentration difference inside the membrane Δc^{int} can be written in terms of the bulk concentration on either side of the membrane $\Delta c^{out} = c^2 - c^1$ by [3]:

$$\Delta c^{int} = K\Delta c^{out}, \tag{2.4}$$

where $K = exp(-\Delta G/RT)$, is the partition coefficient and ΔG is the difference in Gibbs free energy before and after insertion. Although not obvious, this equation is obtained by equating the chemical potential just inside the membrane phase to that on the bulk water side of the interface [2]. Its origin will be discussed further in chapter 5. Combining Eqs. 2.3 and 2.4, we obtain:

$$P = \frac{J}{\Delta c_{out}} = \frac{DK}{d}. \tag{2.5}$$

This defines the diffusive permeability P. Although we have given a derivation for water, it is shown in [2] that this relation holds for most small solutes. The HSDM relates the permeability of a molecular species to its diffusion coefficient inside the membrane, its water/hydrocarbon partition and the membrane thickness. It gives a physical basis for the proportionality between P and KD as well as P and $1/d$ found experimentally.

2.3 Bilayer Structure

Even though the bilayer is not held together by covalent bonds, it is a stable entity over a wide range of conditions. The resistance that the membrane offers to a traversing particle will depend greatly on the distributions of lipid tails within the bilayer. Density profile obtained experimentally from diffraction experiments give information about the distribution of particles at different depths in the membrane. Both atomic and electron density distributions give information about the area and volume per lipid, the thickness of the membrane and the amount of water per lipid at full hydration [26]. The thickness of the membrane is obtained by measuring the distance between the peaks of the electron density profile caused by the electron rich phosphate groups [10]. The density profile is easily obtained from computer simulation by counting the number of molecules in slices along the bilayer normal. Taking an average over the course of a simulation allows for comparison with experimental data.

Studies using nuclear magnetic resonance have revealed the order in the tail sections of lipid bilayer membranes. Ordering and packing of the tails are important factors which affect the transport properties of molecules across BLM. More ordered parts of the membrane will typically offer more resistance to permeation than less ordered parts because the lipid sections in these parts of the membrane are more tightly packed together leaving less room for the penetrating molecule. The chain ordering is usually measured using the order parameter S_{CD} defined by:

$$S_{CD} = \frac{1}{2}\left\langle 3cos^2(\theta_i) - 1\right\rangle \tag{2.6}$$

In computer simulations, θ_i is the angle between the vector pointing from the (i+1)th to the ith bond along the carbon chains and the bilayer normal. The angular brackets denote an average over the ensemble. The subscript "CD" refers to carbon and deuteron atoms used to measure this profile from NMR experiments. Ordered segments will have values close to -0.5 when perpendicular to the bilayer normal or 1 when parallel to the bilayer normal. Unordered bonds will have $S_{CD} \sim 0$.

In a series of articles in the mid to late 90's, Marrink and Berendsen performed simulations studying the permeation resistance of lipid membranes and proposed a four region model to describe the lipid bilayer. This model applies to bilayers in the fluid phase. The regions are described in terms of the ordering properties and density profiles of simulated membranes. The regions, as described in Refs. [25, 27, 28, 26] are:

Region 1: The perturbed water region This region starts where the water layer begins to feel the presence of the bilayer and ends where both water and lipid densities are comparable. It's main features are the head group protrusions out of the bilayer and smooth decrease in the water orientation profile from the interface to the bulk water phase. It is most important in the interactions between two membranes as well as interactions between membranes and proteins.

Region 2: Interphase This is the region with the highest particle density and is approximately $0.8nm$ thick. It starts where region 1 ends and stops where the water density goes to zero. It plays an important role in the phase behavior of the bilayer, and the membrane's elastic properties.

Region 3: Soft Polymer Region 3 is composed mainly of ordered lipid chain segments and resembles a soft polymer in density. It starts where the water density is virtually zero and extends to where the tails have a density equal to that of liquid hexadecane, about $0.8nm$ in thickness. The chain order parameter has a maximum in this region, implying that this is the most ordered region of the bilayer. It is the main barrier to the permeation of small molecules.

Region 4: Decane The fourth region is characterized by a low density and low ordering of the tails. This medium is similar to that of decane. The region is about $1.1nm$ in thickness and spans the center of the bilayer. It is a completely hydrophobic environment.

This model has been cited by a number of studies on lipid bilayers, both experimental and theoretical, on a number of subjects related to lipid membrane. A more elaborate model based on an analysis of the free volume distribution in a simulated membrane has recently been presented [29]. Free volume, or unoccupied volume, is defined as any space which is outside the "interaction radius" of all surrounding particles. Their model divides the membrane into three major zones: the aqueous zone, the polar zone and the apolar zone. Each of these is then subdivided according to the free volume profile of each section. The aqueous zone spans the space where the water first starts feeling the presence of the membrane, the polar zone is the section of the membrane where the head particles spend most of their time. Finally, the apolar zone is the region where the tail particles spend most of their time. Both of these models are based on the time average of the lipids positions on a long time scale, on the order of a few nanoseconds to tens of nanoseconds.

2.4 Inhomogeneous Solubility-Diffusion Model

It has been known since the 70's that the homogeneous description of the lipid bilayer interior assumed by the HSDM is not accurate. The ordered tail regions just behind the head section has been shown to have between 10 to 1000 times higher resistance to the permeation of water than the rest of the bilayer interior [6]. The interior of the bilayer has been shown to offer a much lower resistance to permeation to oxygen [30]. Early works by the authors of [31] used reaction rate chemistry to capture the inhomogeneous nature of the membrane interior. In this model, solute transport is modeled as a point to point hoping process, each hop described by a step size and rate constant. The shortcoming of this approach is the need for all the rate constants.

As mentioned in the previous section, in their studies in the 90's, Marrink and Berendsen introduced the inhomogeneous solubility diffusion model and used it to obtain the resistance to permeation profiles for a series of hydrophobic and hydrophilic particles using MDS. The inhomogeneous solubility diffusion model is based on the idea that the driving force accelerating a particle inside the membrane is moderated by the drag the particle experiences within the membrane (as illustrated in figure 2.2 (a)). The average velocity, u_i of a permeating particle within the membrane is proportional to the negative of the gradient of the thermodynamic potential, μ_i, and inversely proportional to the friction coefficient ξ_i:

$$u_i = -\frac{1}{\xi_i}\nabla(\mu_i) \tag{2.7}$$

As done in [27], we assume water to be our solute and drop the subscripts. The flux of water molecules through the membrane and their average velocity are related by:

$$J = cu_i \tag{2.8}$$

The Einstein equation (EE), given by $D = RT/\xi$, relates the friction coefficient to the local diffusion coefficient. Combining this expression with Eq. (2.7) and Eq. (2.8), we obtain:

$$J(z) = -\frac{c(z)D(z)}{RT}\frac{\partial\mu(z)}{\partial z}. \tag{2.9}$$

From the continuity equation

$$\nabla \cdot \mathbf{J} + \frac{\partial c}{\partial t} = 0, \tag{2.10}$$

it follows that in the steady state, $dJ/dz = -dc(z)/dt = 0$, and therefore J is not a function of z. Rearranging and integrating equation 2.9 over the thickness of the membrane yields:

$$\int_{z_1}^{z_2} \frac{dz}{c^{eq}(z)D(z)} = -\frac{1}{RT}\frac{\Delta\mu}{J}. \tag{2.11}$$

Here $\Delta\mu$=$\mu(z_2)$-$\mu(z_1)$ where $\mu(z_2)$ and $\mu(z_1)$ are the thermodynamic potentials in the bulk on either side of the membrane. Introducing $c*$, the equilibrium concentration of water in the bulk, we can write:

$$J = -\frac{c*\Delta\mu}{R^pRT}, \tag{2.12}$$

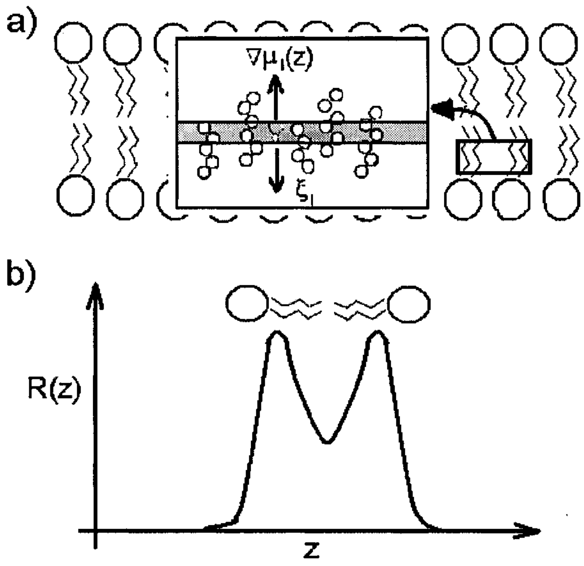

Figure 2.2: a) Conceptual representation of the system used to derive the inhomogeneous solubility diffusion model. On a short time scale, we assume that the water molecule is confined in a region of constant chemical potential so that (EE) is valid. On a longer time scale, we assume that the water molecule is driven by thermodynamic potential $\nabla\mu$. b) Cartoon representation of the resistance to permeation profile $R(z)$ across a membrane as observed from atomistic simulations. Simulations have shown that the region of highest resistance is region 3 of the membrane [27].

where R^p is the permeation resistance defined by:

$$R^p = c^* \int_{z_1}^{z_2} \frac{dz}{c^{eq}(z)D(z)}, \tag{2.13}$$

This quantity is a measure of the resistance the membrane offers to a permeating molecule. It is related to the permeability coefficient of the HSDM by $R^p = 1/P$ as shown in Ref. [27]). No assumptions have been made on the nature of the bulk aside that $\nabla(\mu)$ be constant in the neighborhood of the particle. The ISDM allows direct calculation of the profile of the resistance to permeation knowing the change in concentration with membrane depth as well as the diffusion profile. A cartoon representation of the water resistance profile is shown in figure 2.2 (b).

The interior of the membrane is much more complicated than the simple bulk hydrocarbon assumed by 2.5. The highest permeation barrier is located just behind the head section in regions two and three. A significant decrease is found in the low density section at the center of the bilayer. In a follow up article, the Berendsen group used this method to observe the permeability of a variety of small particles such as ammonia, oxygen and various sized Lennard-Jones particles [28]. Other groups have used this model and obtained the permeation profile of several larger molecules related to cellular functions [32, 33], and anesthetics [34]. In all of these works, the primary objective was to observe the permeation profile of various permeant molecules through a single lipid membrane. In [35], the authors compared the effects of chain branching on the permeation of various small molecules for two different types of lipid membranes.

2.5 Tail Ordering and Free Volume

Tail ordering of the lipids within the bilayer has been shown to be the main barrier to the permeation of most small molecules including water. A prime example of this effect is the size selectivity of the membrane. Xiang and Anderson [22] have presented results on the effects of chain ordering on BLM permeability. They studied the permeation of a series of small molecules of different shapes and found that the HSDM needed to be corrected for chain ordering effects as well as solute shapes [22]. Chain ordering can be induced by cooling the membrane as it goes from liquid to gel, increasing cholesterol content, by changing the lipid heads or by high lateral stress. Other experiments using micropipette aspiration and NMR have both shown that the BLM permeability increases as the degree of lipid unsaturation increases ([20], [23]). Unsaturated tails cause defects in the hydrophobic region, thus decreasing the order in the tail sections. These experimental studies have highlighted the inadequacy of the homogeneous assumption made in deriving the model.

The ISDM of [27] has shed some light on this. According to this numerical study, the barrier to permeation is due to the combination of the free energy barrier in region two and the decreased diffusion through the high density tail section. Water molecules form hydrogen bonded chains that penetrate deep into region two of the membrane. To cross the membrane, a water molecule needs to first undo the H bonds with the other water molecules and diffuse through the dense section of the tails. This process would be facilitated by the addition of kinks in the tail since the deformations would decrease the order in region 3 thus allowing the water particles easier transport across the membrane. Other explanations of the strong dependence of membrane permeability on the tail ordering have been presented in the context of free volume theory. In free volume theory, the permeation process is described in terms of the work needed to create a cavity big enough to accommodate the permeating molecule [36, 37]. Imperfection in region three caused by the kinks in the tails may lead to increased free volume pockets which facilitate the diffusion through this region.

In the work of [38], they showed using MDS that the ordering in the tails decreases as the membrane is stretched. This suggests an increase in the permeability as the membrane is stretched.

Chapter 3 Modeling Membranes

In order to study permeability, a BLM separating two water domains is simulated. The system particles are modeled as beads, distinguishable by their interaction potentials. The dynamics of the system are solved by MDS in the canonical ensemble, that is at constant particle number, constant volume and constant temperature (NVT). In this chapter, the solvent-surfactant model is introduced. I will first discuss the MDS methodology and the initialization procedures. I will then present some results on the self-assembly process and the bilayer density distribution in the liquid crystalline phase.

3.1 Molecular Dynamic Simulations

3.1.1 Potentials and Forces

The most important part of a MDS is the interaction potentials. These define the particles and allow for the observed dynamics. Two classes of MDS have been used in the lipid bilayers; atomistic and coarse grained. In atomistic simulations, molecules are modeled atom by atom as realistically as possible. In coarse grained models, molecules such as water or CH_2 are simplified to spherical group interacting by means of a van der Waals potential. Hydrogen atoms and specific head group molecules are usually neglected. The main advantage of this reduction is to increase the total number of molecules and the overall length of the simulation. A number of coarse grained models have appeared in the last few years with varying degrees of simplification [9, 41, 42, 39, 40, 43]. These have been used to study subjects as varied as protein insertion into a membrane, permeability and phase transitions.

The interaction potentials used in coarse grain MDS are divided into intermole-

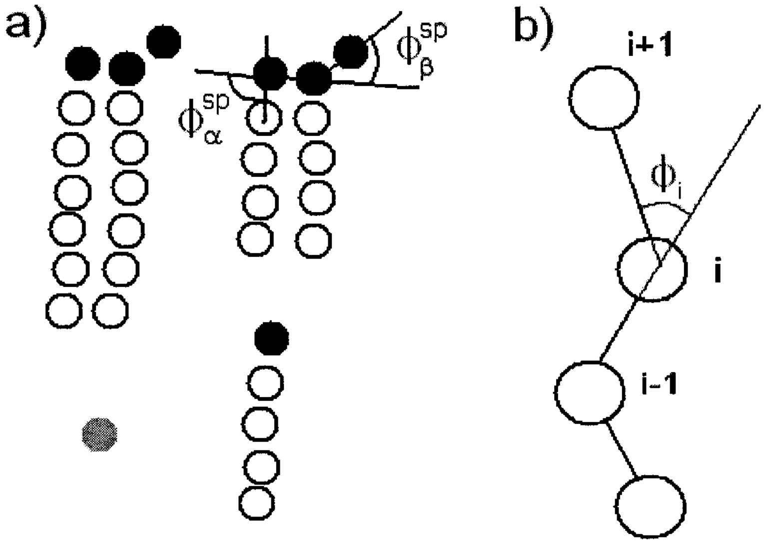

Figure 3.1: a) A cartoon representation of the lipids used in for this thesis,where the solid black circles represent the H beads, hollow circles represent T beads and the gray solid circle represents a W bead. Also shown is the preferred angles for the two tail lipids. b) Illustration of the three body interaction $U_{BA}(\phi_i)$ (adapted from [44])

cular and intramolecular. The intramolecular interaction simulate covalent bonds holding the molecule together. They are usually modeled as rigid spring potentials combined with three body angular potentials which give a shape to the lipid molecules. The intermolecular interaction consist of electrostatic potentials and van der Waals potentials [26].

In our study, we use the model developed by Goetz and Lipowsky [44], a coarse grained MDS, to simulate the BLM/water system. This is a versatile model that has been used to study membrane elasticity [44], bending in lipid membranes [45],[46], the lateral diffusion of lipids within a monolayer [7] and pore formation [47],[48] to name only a few. In this model, the lipids and water are constructed using beads of three types. One representing a hydrophobic (T-beads) molecule, one representing a hydrophilic (H-beads) molecule and the third a water (W-beads) molecule. Three different lipid structures where used in this study; a single tailed lipid, made of a single H bead and $4T$ beads, a double tailed lipid made of three H beads and two $4T$

bead long tails and a second double tail lipid which is the same as the first but with a $6T$ long tail. In the notation presented in [44] HT_4 refers to the single tailed lipid, and $H_3(T_4)_2$ and $H_3(T_6)_2$ refer to the double tailed lipids respectively. All particles and lipid configurations are depicted in figure 3.1.

The intramolecular potentials which hold the lipids together are the harmonic and bond angle potentials. The harmonic spring potential holds the beads at a near fixed distance. The potential is applied to all consecutive monomers in a lipid:

$$U_{HP}(r_{i,i+1}) = k_2 \left(|r_{i,i+1}| - \sigma\right)^2 \tag{3.1}$$

The three body bond angle potential is applied to consecutive triplets of beads as shown in Fig. 3.1. It is given by:

$$U_{BA}(\phi_i) = k_3 \left(1 - cos(\phi_i - \phi_i^{sp})\right) \tag{3.2}$$

The angle preference, ϕ_i^{sp}, combined with the relaxed bond length σ determines the preferred shape of the lipid. The value of the parameters k_2 and k_3 allow for deviations from the relaxed state. We use a spring constant $k_2 = 5000\epsilon$ and a bond angle stiffness $k_3 = 2\epsilon$ except where noted otherwise. Using this value of k_2, the authors of Ref. [44] report that no more than 10 percent of the bonds differed by at most 2 percent of the relaxed bond length, thus producing a near fixed distance between two covalently bonded molecules. The single tail lipid are assumed to be straight so that the preferred angle is set to $\phi_i^{sp} = 0$ for all triplets. For the two tail lipid, we shape the head using the angles $\phi_\beta^{sp} = \pi/6$ and $\phi_\alpha^{sp} = 5\pi/12$ as shown in figure 3.1, while the triplets in the tail have a preferred angle set to $\phi_i^{sp} = 0$. This gives a 2 tail lipid somewhat reminiscent to the one presented in chapter 1.

The intermolecular interactions applied to all particles depend on the particle's "hydrophilicity" (either hydrophobic or hydrophilic). Beads which have the same "hydrophilicity" interact by a Lennard-Jones potential:

$$U_{LJ}(r) = 4\epsilon \left[\left(\frac{\sigma}{r}\right)^{12} - \left(\frac{\sigma}{r}\right)^{6}\right], \tag{3.3}$$

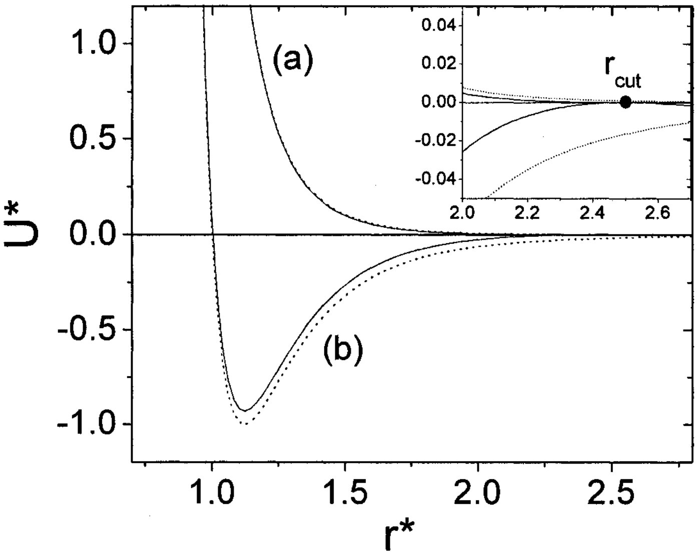

Figure 3.2: Comparison of intermolecular interaction potentials used in the simulation; a) Lennard-Jones, and b) Soft core repulsion. Dotted lines represent the shifted functions where as the full lines show the shifted potentials. The inset shows the effect of the shifted potentials near at the cutoff distance.

whereas those with a differing hydrophilicity interact by a softcore repulsive potential:

$$U_{SC}(r) = 4\epsilon\left(\frac{\sigma_{SC}}{r}\right)^9 \tag{3.4}$$

The Lennard-Jones potentials can be physically interpreted as simulating a dipole-dipole interaction whereas U_{SC} is somewhat arbitrary in form. It mimics the entropic repulsion between hydrophobic and hydrophilic molecules. Other models use a shifted Lennard-Jones potential with a short cutoff as a repulsive potential [9]. The parameter $\sigma_{SC} = 1.05\sigma$ is chosen so that both 3.3 and 3.4 are of similar, but opposite, values from $r = \sigma$. Before this point both functions become positive. For both intermolecular potentials, a cutoff radius is used in order to save on the number of interactions needed to be calculated. Any particles that are more than $r_{cut} = 2.5\sigma$ apart do not interact. Beyond r_{cut}, the intermolecular interactions contribute vary little to the overall potential energy. As shown in figure 3.2, the potentials at r_{cut} are slightly larger than zero. This causes a discontinuous jump $U^*(r_{cut})$. To avoid this, we shift both intermolecular potentials using:

$$U^s(r) = U^*(r) - U^*(r_{cut}) - \left.\frac{dU^*}{dr}\right|_{r=r_{cut}} (r - r_{cut}) \tag{3.5}$$

This insures that both $U^*(r_{cut})$ and $dU^*(r_{cut})/dr$ are zero. We do not apply a cutoff radius to the intramolecular potentials since these potentials are increasing with distance and only involve two or three molecules.

Due to the cutoff radius, most particles in the system won't "see" each other. To avoid having to calculate the interaction between particles that are at a distance greater than r_{cut}, we link the particles to a grid. At the start of a run, we divide our system into cells which are r_{cut} across. Prior to calculating interactions between particles, we link each particle to a cell. Particles only interact with other particles which either belong to the same cell or to an adjacent cell. This implies that we test the radius between particles that are at most $2r_{cut}$ apart.

To obtain the force, we need to take the first derivative of the potential function. This is straightforward for U_{LJ}, U_{SC} and U_{HP} but a bit more involved for U_{BA} due to the three body nature of this potential. In appendix A, we derive the expression of the forces resulting from interactions involving the 2 and 3 body potentials. To save on the computation time, we calculated 200000 values of all interaction energies and forces from 0 to the cutoff radius and stored them in an array at the start of a run. This eliminated the need to make explicit calculations during the simulation.

As is the case for any simulation we must make all quantities diemnsionless. We define the units of energy, distance and mass and express all other variables in terms of these units. Both the energy and distance are expressed in the Lennard-Jones units ϵ for energy and σ for distance. The mass is the third non-dimensionalizing variable which we set at some value m^*. All other units can be defined in terms of these three parameters. Of great importance is the time scale which is given by $\tau = \sqrt{m^*\sigma^2/\epsilon}$.

The values of the length, and time scales are somewhat arbitrary. The same scales described in [44] are assumed in our study. We set the values of ϵ, σ, m^* according the experimentally measured values of $\epsilon = 2kJ/mol$, $\sigma = 1/3nm$ and $m = 36g/mol$.

The value of ϵ is chosen in between the water-water interaction energy and those of CH_2. The distance $\sigma = 1/3nm$ represents the bond length between three to four CH_2 groups. Assuming the size of the beads represents 3 to 4 CH_2 groups we obtain a mass of approximately $m = 36g/mol$. These parameters imply that the water beads represent approximately two water molecules whereas the head and tail beads represent approximately 3 monomers. The chosen parameters are arbitrary and we treat them very loosely. We present our results in non-dimensional form except when comparing with experimental results. Most of the analysis will assume the W beads represent a single water molecule and will be noted otherwise.

3.1.2 Evolution of the Dynamics in the NVT Ensemble

In a molecular dynamic simulations, movement within a system is described by Newton's Laws. Starting from an initial configuration at time t, new configurations a time Δt later are found from the forces and velocities of the present step. Time is discretized in specified steps Δt. The forces exerted on each of the particles are a result of the interactions which were given in the previous section. From the forces, we obtain the accelerations $a(t) = F(t)/m = F(t)$. At each iteration we need to find $\{x(t), y(t), z(t)\}$ and $\{v_x(t), v_y(t), v_z(t)\}$ at a later time for each of the N particles in the system. That is, we need to solve a system of $6N$ differential equations.

The most commonly used algorithm for MDS is the Verlet algorithm. It is obtained by combining the Taylor expansion of the position just before time t, at time $t - \Delta t$, and a little later at time $t + \Delta t$:

$$\begin{aligned} x(t+\Delta t) &= 2x(t) + x(t-\Delta t) + a(t)\Delta t \\ v(t) &= (x(t+\Delta t) - x(t-\Delta t))/2\Delta t \end{aligned} \tag{3.6}$$

which is accurate up to $O(\Delta t^4)$. Although $v(t)$ is not explicitly needed to find the new positions, they are needed to monitor the temperature of the system. In this form, the Verlet algorithm can be cumbersome to use in a NVT ensemble since temperature needs to be controlled using the speed of the particles. To avoid this, we employ a common "trick" by calculating the velocities a half step ahead of the positions. That is:

$$\begin{aligned} x(t+\Delta t) &= x(t) + v(t+\Delta t/2)\Delta t \\ v(t+\Delta t/2) &= v(t-\Delta t/2) + a(t)\Delta t \end{aligned} \tag{3.7}$$

This algorithm is know as the Verlet Leap-Frog algorithm since the velocity and position jump overtop one another after each iteration. To obtain the velocity at time t, we average the values at the two time steps $v(t) = (v(t+\Delta t/2) + v(t-\Delta t/2))/2$. When properly implemented, only the positions at time t, velocities at time $t - \Delta t/2$ and accelerations at time t need to be stored to find the new positions and velocities.

Simulating the canonical ensemble requires holding the temperature, volume and number of particles constant during the course of a simulation. To achieve a constant temperature in the system we use the velocity rescaling technique [11]. According to the equipartition theorem, the average kinetic energy in each direction is proportional to $k_B T/2$. With proper non-dimensionalization, we can express this as:

$$T^* = \frac{1}{3N}\left\langle \sum_{i=1} \mathbf{v}_\mathrm{i}^* \mathbf{v}_\mathrm{i}^* \right\rangle \tag{3.8}$$

where $\mathbf{v}_\mathrm{i}^*$ is the non-dimensional velocity of the i'th particle. Once the temperature is computed using Eq. (3.8), each component of the velocity is rescaled as follows:

$$v_{ix}^{*new} = v_{ix}^* \sqrt{\frac{T_D^*}{T^*}} \tag{3.9}$$

where T_D^* is the desired temperature. The subscripts represent the x'th component of the velocity vector of the i'th particle. After a short initialization period, this algorithm yields a vary stable temperature. This method is the most commonly used in NVT simulations.

Because of the very stiff harmonic spring potential, we cannot use τ as our time step to iterate the MDS. To be assured of a stable algorithm, the time step is set to $t^* = \tau/2000$, or about $7.5 \times 10^{-15} s$. The temperature is also a critical parameter which will determine the phase of the bilayer. Throughout this thesis, we use a constant temperature of $T = 1.35\epsilon$ which was shown to produce a stable bilayer in the liquid crystalline phase. This implies that we are simulating a membrane at a temperature of $324K$ or about $50°C$.

The number of particles in a simulation is limited by the computation time required for the intermolecular interactions. All of the simulations performed were kept below 10^4 particles. The particles are enclosed in an elongated box with an equal lengths along the x and y directions L_{xy}, and a longer normal length in the z direction L_z. The overall particle density $N/{L_{xy}}^2 L_z$ was kept constant at $2/3\sigma^3$. The small number of molecules and small cell sizes introduce artificial boundaries in the system. One way reduce this effect is to apply periodic boundary conditions (PBC) in all three direction in the system. Periodic boundaries repeat the simulation cell in all 26 directions around the primary cell. The primary cell is at the center of a $(3 \times L_{xy}) * (3 \times L_{xy}) * (3 \times L_z)$ box. In this way, a particle near a boundary, say at $x = 0$ will interact with particles near the other boundary, at $x = L_{xy}$ (see [49, 11]). When a particle crosses a boundary, it reemerges on the other side. We must insure that L_{xy} and L_z are much larger than $r_c ut$ so that a particle does not interact with itself. The use of PBC's amounts to simulating an infinite periodic system.

3.2 Initialization

3.2.1 *Starting Configuration*

To generate a stable bilayer we need to pay special attention to the initial configurations. Depending on the overall particle density of the system and the lipid to solvent ratio, spherical and cylindrical micelles may be more favorable structures than the bilayer. Two different starting configurations can be used to initialize the system; either the lipids are placed in random manner throughout the simulation cell and left to self-assemble, or the lipids can be placed in a prefabricated bilayer. For the simulation we carried out to study permeability, we used a prefabricated lipid bilayer.

The preassembled bilayers were built at the center of the simulation box by randomly placing an equal number of lipids in each monolayer. An equal amount of water beads were randomly placed on either side of the membrane. Initial configurations used to obtain the self-assembled bilayers were made by randomly placing lipids throughout the simulation cell. The lipid concentration, defined as the number of lipid beads divided by the total number of beads, was set to a value known to self-assemble into a bilayer (as described in Ref. [44]). Each lipid was "grown" from a starting point along a line in a randomly chosen direction. With all the lipids in place, the water was added randomly throughout the cell. The total number of lipids in the system was set at $N_{lip} = 128$ for the single tail and $N_{lip} = 110$ for the double tail lipids. The number of water particles was chosen such that a density of $2/3\sigma^3$ was maintained near the boundary for all stretched membranes.

Because we use a randomly generated initial configuration, some particles are too close to one another causing large forces which the MDS cannot handle. To avoid this problem, we used a Metropolis Monte-Carlo algorithm (MC) to relax the system. The MC algorithm avoids the problem of large forces because new configurations are randomly generated and the total energy will determine if it is accepted. States with lower energies are much more probable, thus the algorithm will naturally descend until the difference in energy between the new configurations and the old configurations is of the order of k_bT. The total energy of the system in a given configuration, U^{tot} is given by:

$$U^{tot} = \sum_{i \neq j}^{N} U^{s}_{LJ,SC} + \sum_{j=1}^{N_{lip}} \sum_{k=1}^{N_{ch}} U_{HP} + \sum_{j=1}^{N_{lip}} \sum_{k=1}^{(N_{ch}-1)} U_{BA} \tag{3.10}$$

The first term is the sum of the intermolecular potentials which applies to all the particles in the system and depends on the hydrophilicity of the particle. The second and third terms are the intra-chain interactions. The sums are carried out over the number of chains (N_{lip} and the number of consecutive chain elements. A MC test is done in three steps. We first calculate the present energy of the system E_{old} using 3.11. We then select a particle at random and move it a distance Δr in a random direction and calculate the new energy E_{new} of the system. We accept the new configuration if $E_{new} < E_{old}$, otherwise we perform the Metropolis step:

$$U^{tot} = \begin{cases} E_{new} & \Re(0,1) < e^{\left(\frac{-\Delta E}{k_B T}\right)} \\ E_{old} & otherwise \end{cases}, \tag{3.11}$$

where $\Re(0,1)$ is a random number between 0 and 1. Each MC time step consists of N_{tot} MC tests where N_{tot} is the total number of particles. The system quickly relaxes typically after approximately 10^4 MC time steps, where the total system energy is reduced from $\sim 10^{15}$ to $\sim 10^4$. At these values, the energy per particle is low enough that the MDS algorithm can function. Because of the simplicity in the way we generate new states, this MC algorithm is not well suited for long time simulations. It is also slower than the MDS, taking about three times as long per time step. We use the MDS algorithm to reach equilibrium. All samples where first relaxed using $\sim 10^4$ MC time steps.

Once the system has been relaxed, the configurations need to be initialized to reach an equilibrium state. The amount of time needed to attain equilibrium is a critical matter. To estimate the time needed for a prefabricated bilayer to reach equilibrium, we performed several long runs of 10×10^6 iterations from different initial configurations. The potential energy stored in memory every 10^3 time steps. The potential energy quickly flattens out within 10^6 iterations and remained fairly constant for the remainder of the trial. Despite this, we needed to insure that the system was in an equilibrium state. Therefore we use a relaxation time of 2×10^6 iterations as an equilibration period for all samples used. In Ref. [44], they use times of "up to" 3.2×10^6 iterations, but we found no significant difference when using this longer initialization time.

3.3 The Self-Assembly Process

With the chosen overall density and temperature, this model is fully capable of forming a self-assembled bilayer if the box size and lipid to water ratio are properly chosen. We used a system consisting of 100 HT_4 lipids (bond angle potential $k_3 = 0$) with 840 water beads and a box size of $L_{XY} = 12$ and $L_Z = 15$ which gives the required particle density of $2/3\sigma^3$. The choice of these settings was inspired by Ref. [44].

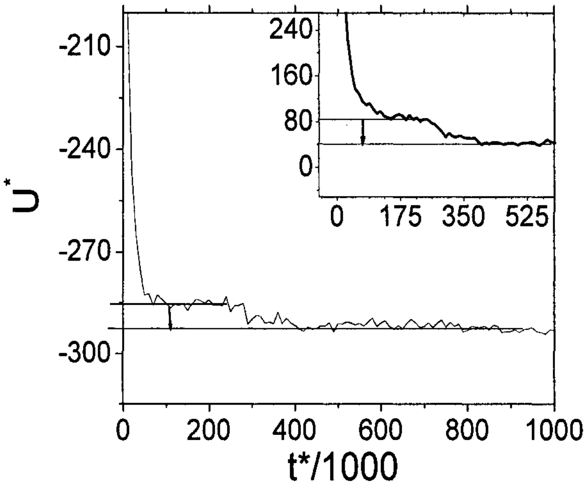

Figure 3.3: Time evolution of the total potential energy of the system. The inset is the first 5×10^5 time steps of the $W - T$ interaction. Note the sudden jump in potential energy of the $W - T$ and total potential energy.

We find that the randomly distributed water/lipid system formed a self-assembled lipid bilayer within 10^6 time steps. The lipids first form a wormlike micelle, which spans the simulation box within the first 10^5 time steps. This structure continued to evolve, for $10^5 - 2 \times 10^5$ iterations up till sometime between the time steps 2×10^5 and 4×10^5 the structure collapses onto a plain with protruding lipids. During the following 6×10^5 iterations, the lipids reorder within the laminar structure. In figure 3.4 we show the a few snapshots of the system before and after these key time steps. A subsequent 10^6 iterations where performed but no qualitative changes in the system where observed.

To understand what drives the self-assembly process we observed the time evolution of the total potential energy, and each of the potentials which make it up. Shown in figure 3.3 is the evolution of the total potential energy and in the inset is the interaction of the $W - T$ beads. Note the sudden drop of the $W - T$ potential at about $t^* \sim 3.5 \times 10^5$ as well as the drop in the total potential energy. This drop occurs in conjunction with the lipids collapse into a laminar configuration (see fig. 3.4). The self-assembly process is first driven by the minimization of the exposer

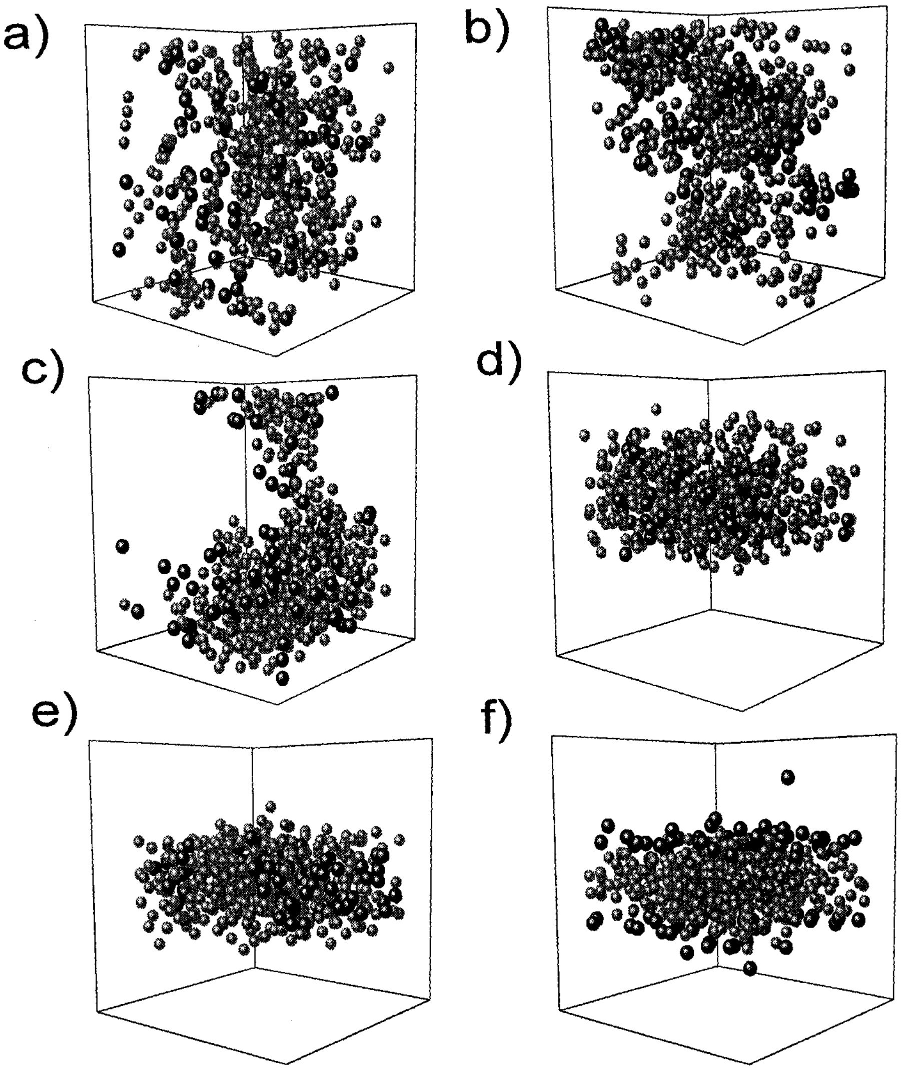

Figure 3.4: Snapshots of the self-assembly process of a the HT_4 ($k_3 = 0$) system containing 100 lipids and 840 W beads (not shown). Black beads are the head particles and the gray beads are the tail particles. Each picture is 13σ by 13σ by 16σ. Times shown are a)$t^* = 0$ (10^4 MC steps), b) $t^* = 10^5$, c) 2×10^5, d) 3.6×10^5, e) 5×10^5 and f) 10^6.

of the tails to water which is quickly minimized. The transition from the wormlike micelle structure to the laminar structure appears to occur in a step like fashion. For the remainder of the simulation, there was little variation in the $W-T$ potential. Once in the layered phase, reordering of the lipid tails and head particles take place in order to further optimize the interaction between the head and tail particles. This occurs on a much longer timescale than the transition from the wormlike micelle to the laminar structure.

3.4 The Liquid Crystal State

At the given temperature and density, the authors of Ref. [44] showed that the lipids diffused laterally within the bilayer. The long time root mean squared displacement of the lipids within a monolayer was found to be proportional to the root of t^* which is typical behaviour for a fluid [11]. They also showed that the value of lateral diffusion coefficient was of the right order of magnitude compared with those found experimentally for each of the lipids used in their study. In order to further characterize this state, we look at the in plane radial distribution function of the center of masses of the lipids. This gives information about the local structure of the bilayer.

To obtain this quantity from simulation we first sorted out the lipids in their respective monolayers, and found the center of mass (CM) of each lipid. We calculate the distance between each lipid CM and store into bins the number of lipids that are between a distance r and $r+dr$. This gives us the right hand summation of Eq. (1.3). Averaging over the course of a 10^6 long simulation we get the RDF. The radial distribution function for a HT_4 lipid bilayer is presented in figure 3.5. Note how there is only one wide peak. The shape $g_{xy}(r)$ is reminiscent of a low density fluid [11], which is approximately what we have here given that the in plane density is $0.4 beads/area$. The lack of other peaks means that there is no long range order. Therefore the lipids are randomly spread across the membrane surface, indicating that we are in the liquid phase.

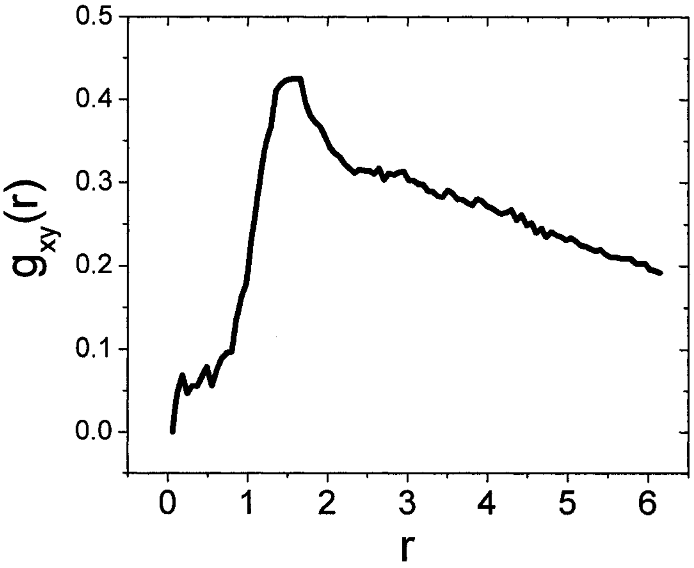

Figure 3.5: The 2D radial distribution function for the TH_4 membrane.

3.5 Density Profile: Dividing up the Membrane

To get a good understanding of the structure of the membrane, we divided the simulation box into slices along the bilayer normal and averaged the number of beads in each slice during the course of a simulation. This method allows us to view a profile of the density of all three types of particles along the bilayer normal. From the profiles, we can define different regions of the membrane. This was done for the bilayers composed of all three lipid geometries and the resulting profiles are presented in figure 3.6. Using this method also allows us to obtain the thickness of the bilayer. We define the thickness as the distance between the maximum in the H particle distribution. The thickness of the membranes measured from these profiles will be presented in the next chapter.

The shorter tailed lipid bilayers composed of the HT_4 and $H_3(T_4)_2$ lipids are very well described by the three zone model proposed in Ref. [29]. The first zone is rich in water and extends out from the membrane into the bulk water to a point where the lipid bilayer is no longer felt. The overall density in this region is nearly constant,

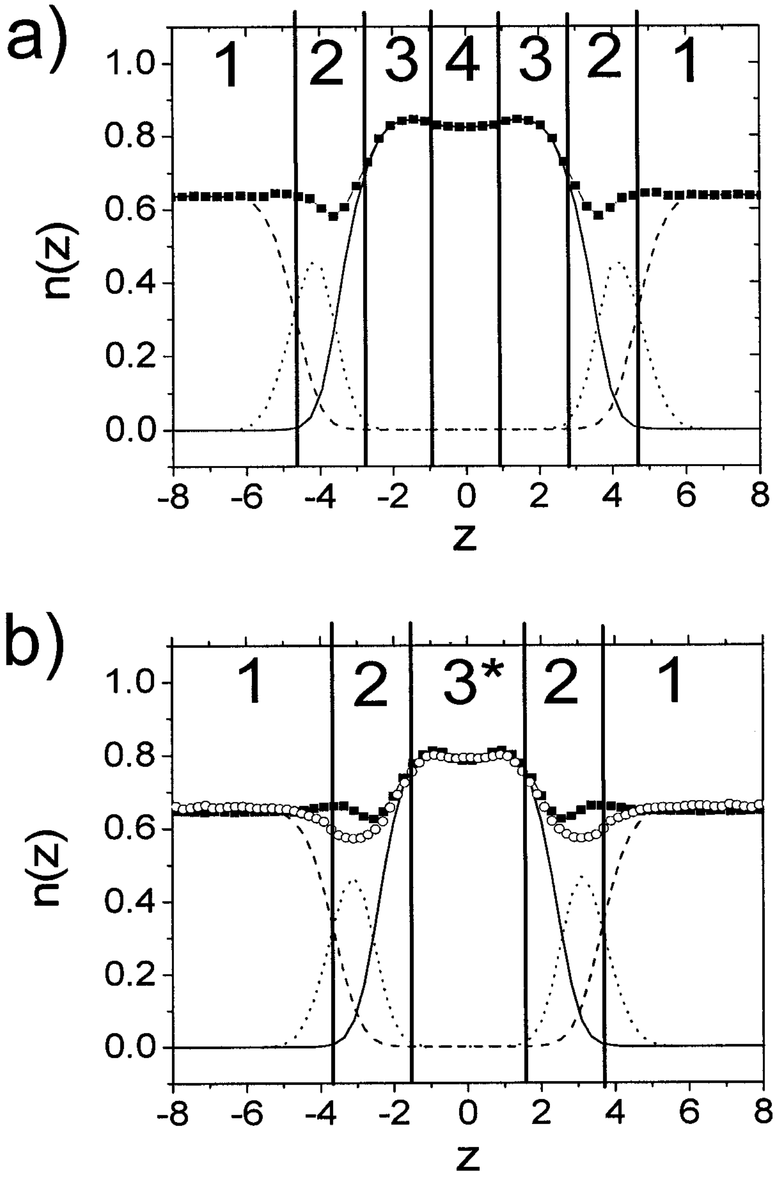

Figure 3.6: Graph a) shows the four region model adapted for the $H_3(T_6)_2$ lipid bilayer and b) shows the three region model for the shorter tail lipids

near the bulk density. In zone 2, we find most of the head groups. This region separates the hydrophobic T beads from the W beads, starting where the head and water beads are of comparable density and extending to where the W bead density is near zero. Because this region is deficient in both of the W and T specimens, there is a dip in the overall density here. The final zone for the short tailed bilayer is the T rich hydrophobic zone. It is here that the membrane density is at its highest. In the case of the $H_3(T_6)_2$ lipid membrane, we use a four region model to describe the membrane. The regions 1, 2 and 3 are the same as those described for the short tailed lipids. We add a fourth region in the center of the membrane where the lipid density dips which describes the membrane interior.

Our four region model is quite different from that of Marrink-Berendsen [25, 27, 28, 26]. In our simulations, region three has the highest density whereas region two has the lowest. Because the head groups in our model are rather small, few W beads visit this region of the bilayer. The strong repulsion between the tails and W beads also means that the tails rarely enter this region. That leaves only the head particles. As the water enters region 2 it needs to undo its H-bonds (or Lennard-Jones bonds for our model) with the other water beads. With a larger head on the lipid, the water molecule would have more sites to bond with making the transition less energetically costly. In our case, a water bead in region two is forced to lie directly against the tails which creates an additional energetic barrier to overcome. Region 4 in our model also differs from that in Ref. [27]. We have a much higher density in this region, the second highest in the system. Our model's shorter chains make this region about 3 times thinner than in Ref. [27]. Region 3 in our model is very similar to region 3 in atomistic simulation. It has about the same thickness (~ 0.7nm verses ~ 0.8nm) and has a high density. In terms of the permeation process, region 3 should still be the limiting barrier just as in atomistic simulations.

Chapter 4 Membrane Elasticity

In this chapter, we present the method used to stretch the bilayers. First introduce some basic concepts in membrane elasticity are introduced. This is followed by a discussion of some results on the elastic properties of the BLM simulated. Original results on the stretching properties of the $H_3(T_6)_2$ bilayer are presented.

4.1 Elasticity Theory for Lipids

The bilayer as a whole is a highly entropic material with distinct elasticity. It can be stretched and bent as shown in figure 4.1. At the lipid/water interphase, there is a surface tension Γ which is measured as the amount of force per unit length of bilayer. As a lateral stress is applied to the bilayer, its response will be characterized by an area compressibility modulus defined as:

$$K_A = A\left(\frac{\delta\Gamma}{\delta A}\right)_T, \tag{4.1}$$

where $K_A \sim 0.14N/m$ [6] is the area compressibility modulus. When no stress is applied, the bilayer will have a preferred area, or tensionless area, A_0. Similar expressions can be written for the bulk volume modulus $K_V \sim 2 \times 10^9 N/m^2$ [6], and the thickness compressibility modulus $K_t \sim 1.4 \times 10^8 N/m^2$ [6]. Dividing by the bilayer thickness, $d \sim 4nm$ [6], the area compressibility modulus can be compared with the values of the bulk and thickness compressibility giving $K_A/d \sim 3 \times 10^7 N/m^2$. This value is an order of magnitude smaller than the thickness compression modulus and two orders of magnitude smaller than the volume compression modulus. The membrane is much more compressible in the lateral direction than in the other two modes of deformation. This allows us to assume that the bilayer is incompressible. In

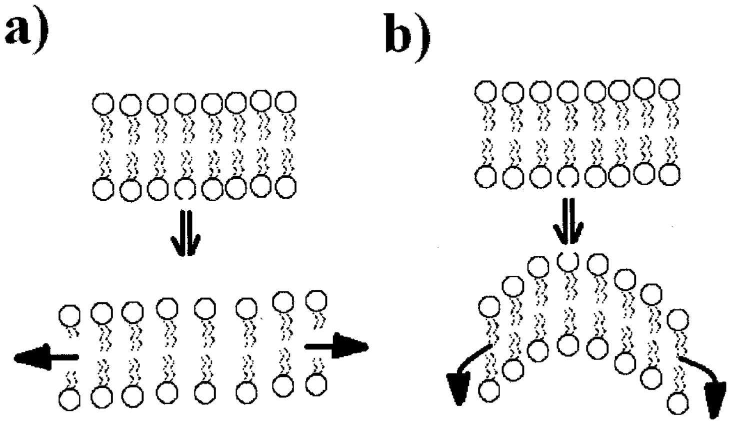

Figure 4.1: Two different methods of deforming a bilayer, a) Stretching and b) Bending

the limit of small area expansion $\Delta A = A - A_0$, one finds a Hooke law type relation between the tension applied to the bilayer Σ and the resulting area expansion [45]:

$$\Sigma = K_A(A - A_0)/A_0. \tag{4.2}$$

If we now consider the membrane to be incompressible, there are no volume changes during the lateral extension. The work done by an external force to expand the membrane an area dA and produce an isotropic tension Σ is given by $dw = \Sigma dA$. Assuming the area expansion is done isothermally, the work done by the external force is equal to the change in surface free energy $dw = dF$. Thus, $\Sigma \sim dF/dA$ and upon integration:

$$\Delta F = \frac{1}{2}K_A(A - A_0)^2/A_0. \tag{4.3}$$

This gives an alternate definition for the area compressibility modulus $K_A = A_0(d^2F/dA^2)_T$. Of course, if a larger tension is applied the membrane will rupture forming either cracks or pores depending on its state [50]. At temperatures of biological relevance, the formation of small pores is most common. Small transient pores are the result of thermal fluctuations and have been shown to be important in the dynamics of membrane rupture [16].

Bilayers can also resist the bending induced by an applied torque. The bending rigidity, κ_b, along with the Gaussian bending rigidity, κ_g, define how the bilayer will respond to an applied torque. The energy per unit area to curve a bilayer is given by [51]:

$$\Delta f = \frac{\kappa_b}{2}\left(\frac{1}{R_1}+\frac{1}{R_2}\right)^2 + \frac{\kappa_g}{R_1 R_2} \tag{4.4}$$

where Δf is the curvature free energy density of the surface and R_1 and R_2 are the principal radii of curvature. For most membranes, the Gaussian curvature term is negligible [51], and Eq. (4.4) reduces to:

$$\Delta f = \frac{\kappa_b}{2}\left(\frac{1}{R_1}+\frac{1}{R_2}+C_0\right), \tag{4.5}$$

where we have added in the term $C_0 = 1/R_0$ which is due to the spontaneous curvature. This term is nonzero when a bilayer is curved in the tensionless state. This might be the case if there where more lipids in one of the sheets of the bilayer. It has been shown both experimentally and by numerical simulations ([9, 45, 52, 51, 53]) that the bending rigidity is related to the compressibility modulus by:

$$\kappa_b = K_A(d_t^2/48). \tag{4.6}$$

where d_t is the thickness of the membrane. Typical values of the bending rigidity have been found to range from roughly $0.15 \times 10^{-19}J$ to $5 \times 10^{-19}J$, or in units of room temperature, $5k_BT_{Room}$ to $110k_BT_{Room}$, where k_B is Boltzmann's constant, depending on the type of lipid which compose the membrane [51]. The small value of κ_b implies that thermal fluctuations can induce oscillations in the membrane. By measuring the amplitude of the shape fluctuations of the bilayer, experimentalists have been able to measure the values of κ_b. Theorists have also exploited this effect and have found $\kappa_b \sim 8 - 10k_BT$ from simulation [45, 9].

4.2 Stretching Method

The stretching procedure was done in such a way as to simulate a quasistatic isochoric process. This was achieved by initializing a series of stretched membranes, all in the same NVT ensemble. Each membrane was stretched by extending the box in the XY direction while compressing the box along the Z direction so to conserve the total volume. These where then relaxed and thermalized as described previously. This gives us a set of membranes each characterized by an area per lipid. The preferred area per lipid, a_0, which corresponds to a membrane in the tensionless state is used as our reference. Recalling expression 4.2:

$$\Sigma = K_A \frac{(a - a_0)}{a_0}$$

where Σ is the interfacial tension and a is the area per lipid. If $\Sigma < 0$ we say the membrane is compressed and if $\Sigma > 0$ we say the membrane is stretched. The value of Σ is calculated from the difference between the normal and transverse components of the stress tensor, which are defined as:

$$\Sigma = \begin{pmatrix} \Sigma_T & 0 & 0 \\ 0 & \Sigma_T & 0 \\ 0 & 0 & \Sigma_N \end{pmatrix}. \tag{4.7}$$

Both Σ_T and Σ_N depend on the normal coordinate z only because of the symmetry in the x and y directions. We define the stress profile along the bilayer normal as $s(z) = \Sigma_T(z) - \Sigma_N(z)$, and summing all the contributions along the normal leads to an expression for Σ:

$$\Sigma = \int_{-\infty}^{\infty} [\Sigma_T(z) - \Sigma_N(z)]\, dz. \tag{4.8}$$

By assuming that the macroscopic stress tensors are approximately equal to the thermally averaged microscopic stress tensor then $\Sigma_N(z)$ is approximately equal to $\langle \sigma^{zz}(z) \rangle$ and $\Sigma_T(z)$ is approximately equal to $\langle \sigma^{xx}(z) + \sigma^{yy}(z) \rangle / 2$. The values of the microscopic stress tensor can by obtained from simulation by slicing the simulation

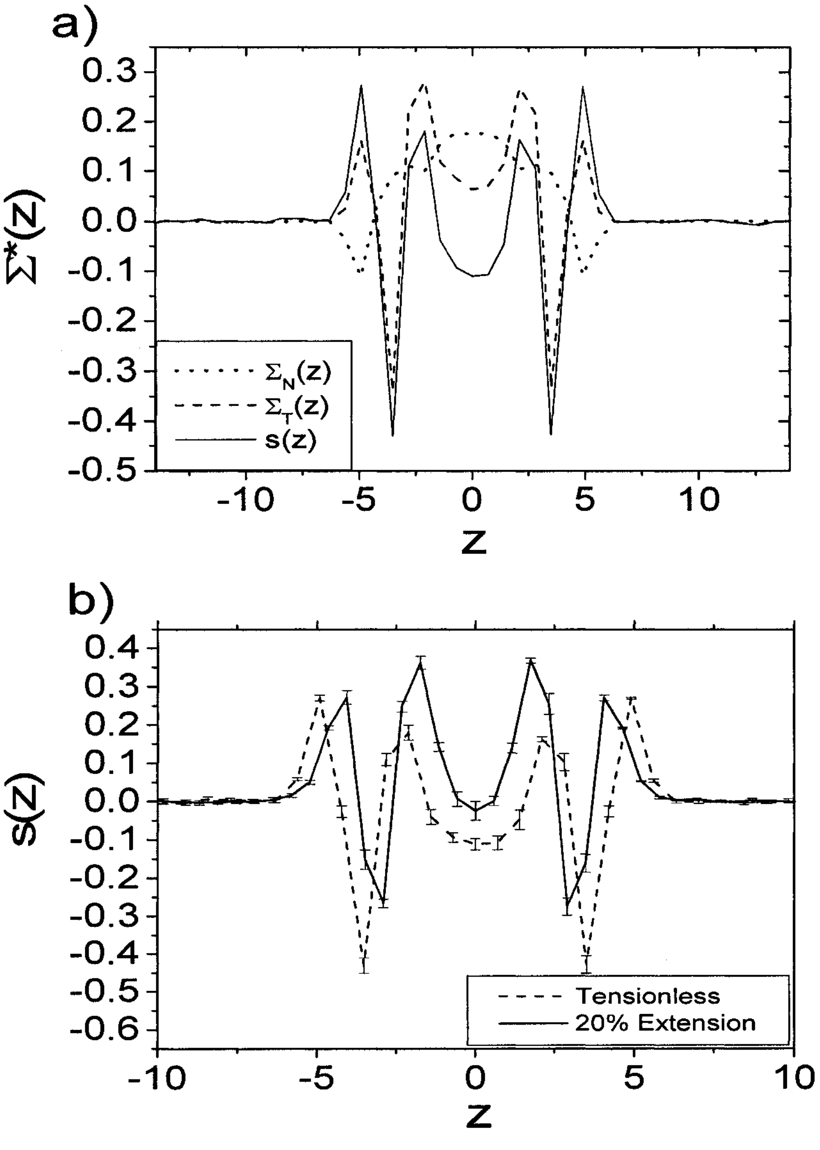

Figure 4.2: a) The contributions of the z-dependent lateral and normal stress tensors to the overall stress profile. The Σ_N and Σ_T have been shifted for clarity. b) Comparison of the stress in the membrane in the tensionless state and at a relative extension of 20%.

box along the z axis and computing, for each box, a modified version of the familiar pressure tensor $P^{\alpha\beta} = \sum^{N} m v_i^{\alpha} v_i^{\beta} + 1/2 \sum_{i \leq j} r_{ij}^{\alpha} F_{ij}^{\beta}$. The modifications to this expression however are not straightforward and the reader is referred to ref. [44] for details. The stress in box i due to two particles whose z coordinates are confined to box i will interact according to $P^{\alpha\beta}$. The novelty of the work by the authors in [44] is the addition of the function $f(z_{j_1}, z_{j_2}, z)$ which scales the contributions of the stress in box i due to the particles which lie outside box i. In the two body case, the value of the z-dependent stress tensor is:

$$\sigma^{\alpha\beta}(z) = \frac{1}{V_{\triangle z}} \sum_{i=<j>} (\nabla_{j_1 j_2}^{\alpha} U) r_{j_1 j_2}^{\beta} f(z_{j_1}, z_{j_2}, z), \tag{4.9}$$

where α, β represent the $\{x, y, z\}$ components of the vectors $\nabla_{j_1 j_2} U$ and $r_{j_1 j_2}^{\beta}$, j represents an interaction between pairs of particles and the function $f(z_{j_1}, z_{j_2}, z)$ scales the contribution of the interaction between particles j_1 and j_2 separated by n boxes. Both the contributions of the 2 and 3 body potentials go into calculating $\sigma^{\alpha\beta}(z)$. For the simulation carried out,

$$f(z_{j_1}, z_{j_2}, z) \sim 1/N_{slice}, \tag{4.10}$$

where N_{slice} is the number of slices between interacting particles. A similar expression is obtained for the three body potentials. In that case, the sum $< j >$ would be over triplets, and a second sum would be needed to included the three possible interactions within a particle triplet. Note that the kinetic part which is usually included in the stress tensor has been omitted. This is because it would cancel out in Eq. (4.8) (i.e. the contribution of the kinetic part due to $\Sigma_N(z)$ would be the same as that from $\Sigma_T(z)$). Samples of $\sigma^{\alpha\beta}(z)$ where averaged over 5000 iterations. These averages were then used to calculate $\Sigma_{\alpha\beta}(z)$. The final value of $\Sigma_{\alpha\beta}(z)$ for a run represents the average over 200 samples. Several independent runs were performed to be assured that the averages represent a good sampling of the configurational space available to the particle. This procedure was repeated for a series of bilayers at different a_0.

In figure 4.2, we show the resulting stress profiles for the bilayer composed of the

Table 4.1: Values of K_A, a_0,κ_b and d_t measured for the different lipid bilayers studied

Lipid	K_A (ϵ/σ^2)	a_0 $(\sigma^2/lipid)$	d_t (σ)	κ_b** (ϵ)
H$T_4(k_3 = 0)$	11.39 ± 0.24	2.31 ± 0.11	5.39 ± 0.5	6.90
H$T_4(k_3 = 2)$	14.96 ± 0.42	2.11 ± 0.08	5.80 ± 0.5	7.98
H$T_4(k_3 = 5)$	11.35 ± 1.13	1.95 ± 0.14	6.5 ± 0.5	9.99
$H_3(T_4)_2$	9.30 ± 0.63	4.15 ± 0.10	6.30 ± 0.5	7.69
$H_3(T_6)_2$	11.39 ± 1.54	4.34 ± 0.19	8.70 ± 0.5	17.96
Experimental*	7.2 (240 mJ/m^2)	5.85 (0.65 nm^2)	10.5 (3.5nm)	24.1 (0.8 $\times 10^{-19}$ J)

*All values are expressed in the non-dimensional parameters discussed in Chapter 3. *Experimental values quoted represent "typical" elastic constants for phopholipids as presented in Ref. [53]. **Values of κ_b calculated using Eq. (4.6)*

$H_3(T_6)_4$ lipids. The stress is concentrated near the water/lipid tail interphase and is mainly due to the contributions from $\Sigma_T(z)$ which has a sharp dip and maximum around 4σ from the bilayer center. Contributions to $\Sigma(z)$ from the normal component are much smoother across the boundary, but make a more significant contribution near the center of the bilayer. As the membrane is stretched, it compresses so that the membrane interior, where the stress is zero, shrinks and the interphase is spread out over a greater percentage of the membrane. This will become important when considering the effects of stretching on the region 4 model. The integral of these profiles yields the interfacial stress of the membrane.

The curves of Σ as a function of the area per lipid are presented in figure 4.3. A linear behavior is observed for small extensions for both the single and double tail lipids. By fitting a line to these curves, we obtain the values of a_0 and K_A as described by 4.2. In table 4.2 we present the values of a_0 and K_A for each of the membranes used in this work along the experimentally obtained values. We also present the relaxed thickness d_0. Because of the different averaging techniques used,

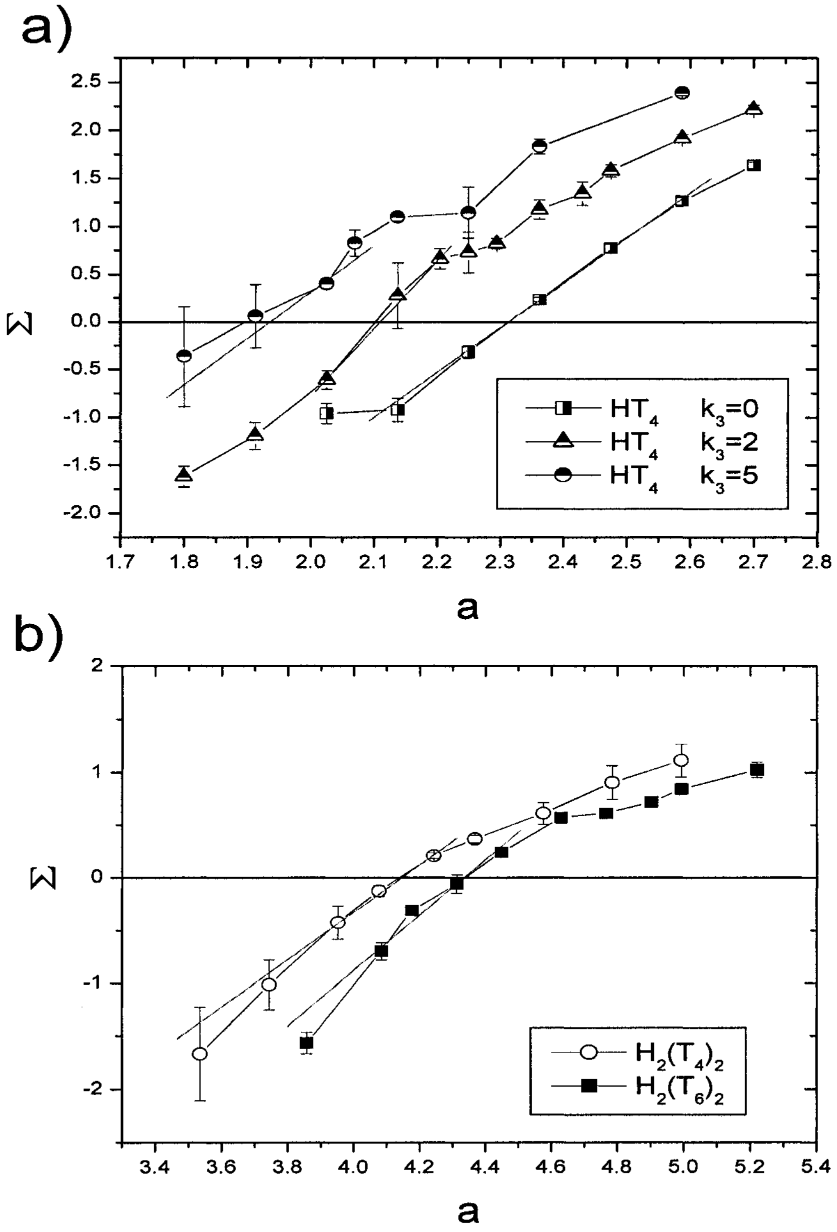

Figure 4.3: Stress as a function of area per lipid for a) single tailed lipid membranes and b) double tailed lipid membranes. Values of the slopes and y-intersection are given in table 4.2

we find slightly different values than those given in Ref. [44]. They obtained values of 13.6 ± 1.6, 11.8 ± 1.5, 12.2 ± 1.6 for the HT_4 $k_3 = 0, 2, 5$ respectfully and 14.3 ± 2.0 for the $H_3(T_4)_2$ lipid bilayer.

Although most lipid membranes are known to spontaneously rupture at about 4 percent relative stretch [16], we were able to stretch our membrane up to about 20 percent without observing rupture. Using the same model we have used here, the authors of Ref. [48] found that the maximum expansion the simulated membrane can support before rupture scales as $\Delta a/a \sim N_{lip}^{-1/3}$. This scaling law implies that for our systems, which contain either 128 (single tail) or 110 (double tail) lipids, rupture should occur at about $20 - 25$ percent relative expansion. We tested bilayers with initial configurations at relative extensions above 25 and found that most developed a pore. A patch of membrane of macroscopic size is about $1 \mu m^2$ and contains on the order of 10^6 lipids [1]. The present scaling law predicts that such a membrane would support a maximum extension of 1 percent. This is very near the 4 percent spontaneous rupture point observed experimentally, or at least on the right order of magnitude [16, 48]. Actually at those sizes, previous studies in our group have shown that a different scaling law applies [16, 54], namely $1/N$.

Chapter 5 Permeability in the Tensionless State

The water permeability of the simulated bilayers was calculated using the inhomogeneous solubility diffusion model introduced in chapter 2. This model relates the flux to a driving force by Eq. (2.12). The permeation resistance R^p was defined and related to the experimentally determined permeability by $P = 1/R^p$. Recalling Eq. (2.13):

$$R^p = c^* \int_{z_1}^{z_2} \frac{dz}{c^{eq}(z)D(z)}$$

we can obtain the permeability of the membrane by calculating the diffusion and concentration as a function of the depth in the membrane. This method will allow us to obtain the overall permeability, a mechanism which occurs on the millisecond timescale, using data measured at the nanosecond timescale. We first need to rewrite Eq. (2.13) since the concentration profile at the center of the membrane cannot be obtained during a simulation of only a few nanoseconds. In a typical run of $1-10ns$, the W beads visit the interior of the bilayer rarely, if at all. To get statistically relevant results, we need to relate $c^*/c^{eq}(z)$ to another observable quantity which can be calculated during a run on this timescale.

The difference in Gibbs free energy of a water molecule at position z in the membrane relative to the bulk, $\Delta G(z)$, is related to the constrained partition function $Q'(z)$ [35]:

$$Q'(z) = \int dr_1 ... dr_n \delta(z' - z) \exp(-V/RT). \tag{5.1}$$

In words, the constrained partition function is the probability that the system resides in a state where the z coordinate of a water molecule is constrained between z and

$z + dz$ [27]. By definition,

$$\Delta G(z) = -RT \ln(Q'(z)/Q'(z^*)), \tag{5.2}$$

where z is a position in the membrane and $z*$ is a position in the bulk. Applying the definition of the partition function:

$$\Delta G(z) = -RT \ln \left(\frac{(akT) \int dr_1 ... dr_n \delta(z' - z) \exp(-V/RT)}{(akT) \int dr_1 ... dr_n \delta(z' - z*) \exp(-V/RT)} \right) = -RT \ln(P(z)/P(z*))$$

It is straightforward to see that the probability of finding a particle at position z relative to the bulk is directly proportional to the ratio of concentrations so that:

$$\Delta G(z) = -RT \ln \frac{c^{eq}(z)}{c^*} \tag{5.3}$$

Rewriting 2.13 in terms of the Gibbs free energy profile ΔG gives us:

$$R^p = \int_{z_1}^{z_2} \frac{e^{\Delta G(z)/RT} dz}{D(z)}. \tag{5.4}$$

Both $\Delta G(z)$ and $D(z)$ can be obtained from a short timescale simulation. In the next two sections, the computational techniques used to calculate these profiles will be introduce. Section three discusses how the profiles are combined in order to get the $R(z)$ profile. In the last section, the overall permeability calculated from our simulated membranes are compared to experimentally determined values of permeability.

5.1 The Free Energy Profile

To obtain the free energy profile across the membrane, two different techniques are used. The most straight forward is to apply 5.4 directly. The constrained particle (CP) method [27] is used in regions where W beads don't visit as often. The two profiles are then combined to obtain the overall free energy profile across the membrane.

5.1.1 Density Ratio Method

The density ratio (DR) method relies on equations 5.3. We sliced the system along the bilayer normal and count the number of W beads in each slice. This process is repeated every 50 iterations, and the totals are averaged at the end of the run. Because each box is of equivalent volume, 5.3 can be rewritten in terms of the particle density $n(z)$:

$$\triangle G(z) = -RT\ln(n(z)/n(z^*)) \tag{5.5}$$

where $n(z^*)$ is density in the bulk. As discussed in Ref. [27], the error associated when using this method is proportional to $1/(nN)^{1/2}$, where N is the number of particles and n is the number of configurations used to average the profile. We limit the use of this method to sections where the density of W beads is greater than 20 percent of the total particle density. During a run of 1×10^6 time steps, we get good enough statistics to obtain $c^{eq}(z)$ in the bulk and near the interphase. The error bars were estimated from the standard deviation of independent runs.

5.1.2 Constrained Particle Method

In the regions where the water particles don't visit very often, we use the constrained particle (CP) method to obtain the missing values of $\triangle G(z)$. Taking the derivative of Eq. (5.2):

$$\frac{d\triangle G}{dz} = -\frac{RT}{Q'(z)}\frac{dQ'(z)}{dz}$$

and applying the definition of $Q'(z)$ we get:

$$\frac{d\triangle G}{dz} = -\frac{aRT}{akT}\frac{\int dr_1...dr_n\delta(z_0-z)\frac{dV}{dz_0}\exp(-V/RT)}{\int dr_1...dr_n\delta(z_0-z)\exp(-V/RT)}$$

$$\frac{d\triangle G(z_0)}{dz} = -<F_z(z_0)> \tag{5.6}$$

where $< F_z(z_0) >$ is the average force exerted on a particle constrained to the position z_0. $\triangle G(z)$ is then obtained by a simple integration. The constrained particles

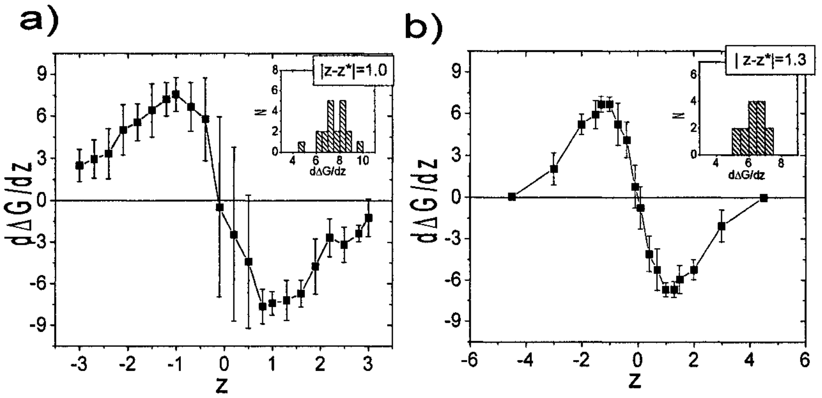

Figure 5.1: Effects of averaging on the $d\Delta G(z)/dz$ profiles. a) Single simulation of the $HT_4(k_3 = 0)$ lipid bilayer. Monolayers where not averaged. b) Average of 4 simulations of the $HT_4(k_3 = 2)$ lipid bilayer. Insets show the distribution of sample values near the maximum of $d\Delta G(z)/dz$.

interact with the surrounding beads and are free to diffuse in the xy plane. During a "simulation", we placed W beads at different depths in the membrane and constrained them to lie in the plane $z = z_0$ for the duration of the simulation. At each iteration, we rescaled the system positions so that the center of mass of the membrane is kept fixed in the center of the cell. Then, the distance between the particle and the center of the cell is kept constant. A similar technic is discussed in Refs. [27, 32].

The initial insertion of the constrained particle was done in such a way as not to "shock" the system. If a particle is naively inserted randomly into the membrane, it may be placed unphysically close to other particles and cause an overestimate of the force $< F_z(z_0) >$. To avoid this, the interaction potential of 100 random sites in the z_0-plane were tested while the system was kept still. Each insertion was relaxed for 10^3 iterations in the fixed configuration using a modified MDS. The system particles were not allowed to move. Only the inserted particle was iterated allowing it explore the surface for the most energetically favorable location. The test bead with the lowest energy out of the sample of 100 was selected for the constrained particle method. We then relax the system containing the inserted bead for 10^4 iterations. Relaxation times of up to 10^5 iteration where tried but no noticeable improvement was observed.

Each simulation was divided into 9 runs and each run divided up into 10 trials. During a run, we place two particles in opposing monolayers (minimum separation between inserted beads was set at 3.5σ) thereby cutting the length of simulation by a factor of two. A single trial had a length of 10^5 iterations during which we averaged the z component of the force on CP every 50 iterations, producing a single value for this time span. We averaged the resulting 2000 samples giving us a value of $d\Delta G(z_0)/dz$. Repeating this procedure 10 times produced the results for a run at a single constrained value z_0. We then start over, placing particles at two new positions within the membrane. The 9 runs yield a total of 18 values of $d\Delta G/dz$ inside the membrane. This method is very processor intensive. On a $2.8Ghz$ pentium processors, it took approximately 170 hours of processing time for the single tails and up to 385 hours of processing time for the $H_3(T_6)_2$ lipid bilayer to perform the necessary averaging in a simulation. Attempts were made to run the insertions in parallel, using 18 processors (one for each particle insertion) but this proved to be manually time consuming.

In figure 5.1 a), the resulting profile $d\Delta G(z)/dz$ for a $HT_4(k_3 = 0)$ system are shown. Note the large error bars despite the 9.0×10^6 iterations used during the simulation. The error bars were determined from the standard deviation of the 10 samples for each insertion position. Also shown is a typical distribution of the 10 points gathered during a run. Note the wide spread of data points. To improve the statistics, the membrane sides were averaged together and at least 3 independent runs were repeated. Therefore, the averages represent a minimum of 60 different samples. Figure 5.1 b) shows a plot of $d\Delta G(z)/dz$ calculated in this way. Note the reduce error bars which were calculated using the two side of each of the independent simulations. The curve is also much smoother owing to the increased amount of data used to compute it. The resulting free energy profile is obtained by integrating the $\Delta G(z)/dz$ from one side of the membrane to the other:

$$\Delta G(z) = \Delta G(-z_1) - \int_{4.5}^{-4.5} \langle F_z(z) \rangle dz$$

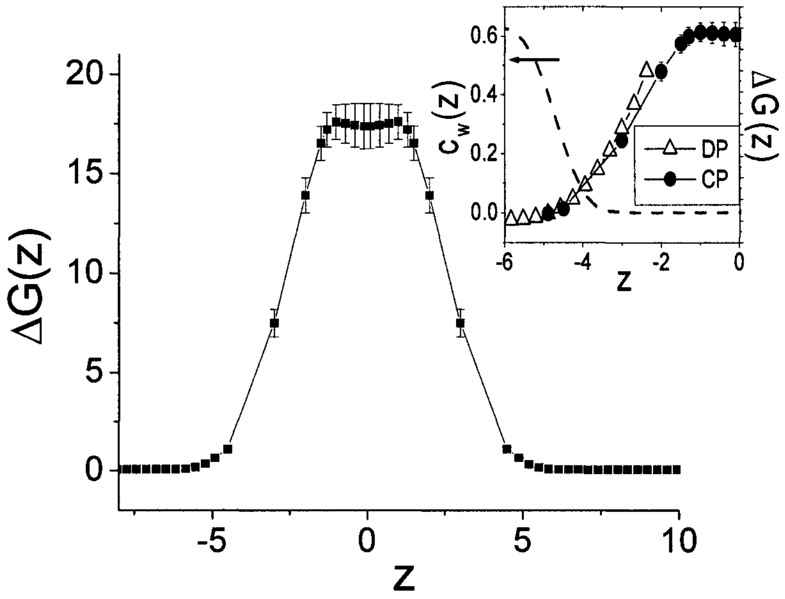

Figure 5.2: The resulting free energy profile for the $H_3(T_6)_2$ lipid bilayer. Inset is the crossover point from the DR method (open triangles) to the CP (full circle). Also shown in the inset is the water concentration $c_w(z)$.

The average force profile, $\langle F_z(z) \rangle$ was calculated up to $\pm 4.5\sigma$ on either side of bilayer. We obtain the initial value $\Delta G(-z_1)$ from the density profile data. The value of $-z_1$ is chosen such that $d\Delta G(-z_1)/dz$ can be assumed to be 0. The integration was performed using the trapezoid method. The error associated with the integration method is much less significant than the standard deviation in each sample.

5.1.3 Combining Methods: $\Delta G(z)$

The $\Delta G(z)$ profiles obtained from each method are combined in such a way as to minimize the overall error. We use the DR method in regions where the water concentration was at least 20 percent of the bulk and the CP method everywhere else. This defines the crossover point, z_c. In terms of z_c, the overall free energy profile is given by:

$$\Delta G(z) = \Delta G^{DR}(z \leq (-z_c)) + \Delta G^{CP}((-z_c) \leq z \leq z_c) + \Delta G^{DR}(z \geq z_c), \qquad (5.7)$$

where we take the center of the membrane as the reference point. In Fig. 5.2 we show the free energy profiles obtained for $H_3(T_6)_2$. The error bars again represent the average between independent runs. Similar trapezoidal shapes were found for membranes composed of $H_3(T_4)_2$, $H_3(T_6)_2$, and HT_4 (see Figs. 5.6, 5.7 and 5.5). The inset of Fig. 5.2 is a comparison between the DR and CP methods around z_c which is located at approximately 3.8 from the center of the membrane. Good agreement is found between the two methods across the transition point. The most significant errors to the profile are due to the CP method.

In atomistic simulations, the Widom particle insertion method is applied to calculate the free energy in areas of low density such as region four at the center of the membrane. This method consists in randomly inserting a "test" particle in the bilayer and calculating its interaction potential with the other beads (see Ref. [11]) without disturbing the configurations. Averaging over a large number of insertions, the excess chemical potential in a given region of the system is obtained. However, if the density of the system is too high, the "test" particle has a high probability of being placed unphysically close to the system particles, overestimating the average interaction potential. Preliminary simulations revealed this to be the case, therefore we could not use this method to calculate $\Delta G(z)$.

5.2 The Diffusion Profile

The diffusion coefficient of interest here is the "local" diffusion coefficient, representing movement on a short time scale. In this sense, we consider water particles confined to a region of thickness dz. Two methods are used to find the diffusion coefficient, the mean squared displacement of the water particles in the system and the force autocorrelation function of a constrained particle.

5.2.1 Mean Squared Displacement

The mean squared displacement (MSD) of the W bead in the neighborhood of the fixed position z_0 is related to the one dimensional diffusion coefficient by:

$$D(z) = \lim_{t \to \infty} \frac{\langle [z(t) - z(0)]^2 \rangle}{2t} \tag{5.8}$$

We are interested in the diffusion on a short time scale, so we only consider the mean squared displacements over a time of 5000 iterations which corresponds to about 3ps. During a run, we averaged the mean square displacements of the beads whose geometric center of displacement is confined between z and $z + \triangle z$. The values of the beads mean square displacements were stored in an array. At the end of the simulation, a least square algorithm was used to determine the diffusion coefficient in each slice. Because the position at time $t = 0$ is arbitrary, we improve the statistics during the run by using a number of time origins.

This method can only be used in regions where the particle density is high enough to allow for sufficient sampling. Therefore, we use this method in the same regions that the DR method was used to calculate the free energy profile. Previous studies found that a single time scale can create a small bias in the value of the diffusion coefficient ([27], [35], [32]). To verity this the mean squared displacement over times between 2000 and 10000 iterations in the bulk and region 1 of the membrane were calculated but the diffusion coefficient was found to vary little (see also ref. [35]).

5.2.2 Force Autocorrelation

Inside the membrane, where water particles don't penetrate, we make use of the force on a constrained particle a second time to calculate the diffusion profile $D(z)$. According to the fluctuation-dissipation theorem, the autocorrelation of random forces acting on a molecule is related to the time-dependent, or dynamic, friction coefficient by [27]:

$$\xi(z,t) = \langle \triangle F(z,t) \triangle F(z,0) \rangle / RT \tag{5.9}$$

Here, the random forces are the fluctuations of the instantaneous force from the thermally averaged force at time t:

$$\triangle F(z,t) = F(z,t) - \langle F(z,t)\rangle \tag{5.10}$$

According to the Einstein equation, the diffusion coefficient at position z is related to the static friction coefficient by $D(z) = RT/\xi(z)$. The static, or time independent, diffusion coefficient is obtained from the integral of the dynamic diffusion coefficient:

$$\xi(z) = \int\limits_0^\infty \frac{\langle \triangle F(z,t)\triangle F(z,0)\rangle}{RT} dt \tag{5.11}$$

Here it is assumed that $\xi(z,t)$ is large and decays on a much shorter time scale than other mechanisms in the system. This assumption assures that the particles stays in a region of constant free energy during the decay time of the friction coefficient, an assumption which is assured if the ISDM is valid. Then the diffusion coefficient is given by:

$$D(z) = \frac{(RT)^2}{\int\limits_0^\infty \langle \triangle F(z,t)\triangle F(z,0)\rangle dt} \tag{5.12}$$

During a simulation, the force F exerted on the constrained particle at time t, relative to a time origin, t_0, was stored in an array $F(\tau)$ where $\tau = t - t_0$. Repeating for each constrained position z_0, we get the values for $F(z,t)$ which are used to find the random force defined by eq. (5.10). We used $t_{max} = 5000$ iterations as the maximum length of each sample used to calculate the correlation function (i.e. $\tau \leq t_{max}$). The same sampling technique used to calculate the free energy is used here. We calculated 10 samples each with 100000 iterations and stored $\xi(z,t)$ at the end of each trial. The ten samples of $\xi(z,t)$ were averaged. The resulting correlation function for the $HT_4(k_3 = 0)$ membrane are presented in figure 5.3.

The averaged $\xi(z,t)$ at two locations in the membrane are presented: one near the interface and the other near the center of the bilayer. The initial value is slightly larger in the center of the membrane, reflecting the inferior diffusion coefficient in

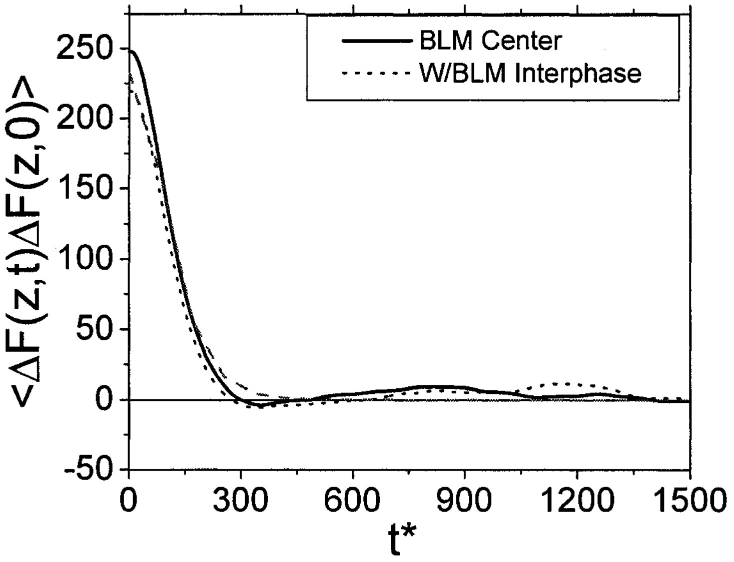

Figure 5.3: Correlation function $\xi(z,t)$ used to obtain the diffusion coefficient. The solid line is from the center of bilayer and dashed line is near in region 1. In gray is fit C(t) to the BLM center data.

that region. Note the fast decay time for both membrane regions, about equal to 300 iterations. We did not observe any significant difference in decay times in the other regions of this (or other) simulated bilayers.

Integration of the autocorrelation function was done in two ways; simple numerical integration and using a fit. The fit adopted was a double exponential of the form:

$$C(t) = C_1 \exp(-t/\tau_1) + C_2 \exp(-t/\tau_2), \tag{5.13}$$

where C_1, C_2, τ_1 and tau_2 were the optimized parameters. Substituting 5.13 into 5.12 and integrating gives:

$$D(z) = (RT)^2/(C_1\tau_1 + C_2\tau_2). \tag{5.14}$$

Fits were done using Microcal Origin software. The quality of the fit was estimated by minimizing the Chi squared of the distribution. The values of diffusion found this way depended greatly on the fitting parameters. We observed values ranging from

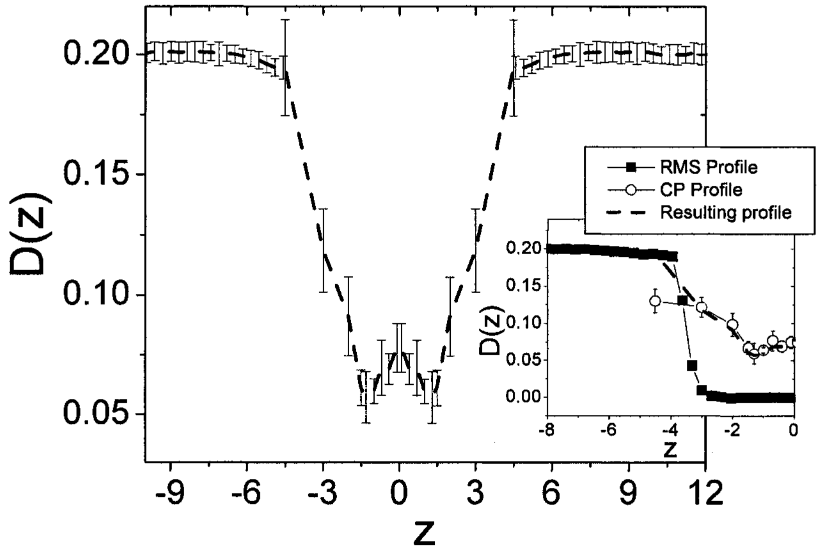

Figure 5.4: The resulting diffusion profile for the $H_3(T_6)_2$ bilayer

$D(z) = 0.10 - 0.13$, for $\chi^2 \leq 30$. The optimizer seemed to easily get caught in local minimums, a problem also reported in [32]. We did observe that the value of the diffusion coefficient seemed to diminish as the fit became better. Given that the observed decay time is of the order of $\sim 10^2$ iterations and $\langle \xi(z,t) \rangle$ was calculated up to 5000 iterations, we can integrate $\langle \xi(z,t) \rangle$ directly using the trapezoid method. The values found using this method were slightly smaller than those using the fitting procedure, but well within the error bars. The nine different locations allowed us to obtain a good profile of the diffusion inside the membrane.

5.2.3 Combining Methods: $D(z)$

To combine the MSD and the force autocorrelation methods, we used the same crossover point that was discussed in section 5.1.3. This posed little problem in the shorter tailed lipid bilayers HT_4 and $H_3(T_4)_4$ where the methods overlapped. However, in the case of the $H_3(T_6)_2$ lipid bilayer, some disagreement between the MSD and CP methods was found at the crossover point. The diffusion found using the CP method was about almost 30 percent smaller than the one found using the MSD. This is shown in the inset of figure 5.4. We assume a linear changeover from the MSD method to the CP method near r_c. This allows a smoother transition from one method to the other which is more probable than a steep drop.

The profiles show that the diffusion is position dependent inside the membrane. This was also observed in atomistic studies ([27], [35], [32]). Interestingly, our results are more consistent with those of Refs. [35, 32] than those in Ref. [27]. The former studies [35, 32] found that the diffusion is a bit less than half the value of the bulk diffusion coefficient at the center of the membrane. They also report a sharp drop in the diffusion across region 1. This is in contrast with the profile discussed in Ref. [27] where the diffusion coefficient for water at the center of the membrane was higher than that in the bulk. In any case, while the absolute value seems to be very dependent on the intermolecular potentials used in the simulation, the overall shape of the profile is constant; a drop starting in region 1 and continuing sharply through region two, followed by a minimum in region 3 and an increase in region 4. This is what is seen in fig. 5.7.

5.3 Membrane Permeability

5.3.1 Permeation Resistance

Having computed the $\Delta G(z)$ and $D(z)$ profiles across the membrane, we can compute the permeability of the bilayer using Eq. (5.4). We first construct the resistance to permeation profile $R(z)$ defined by:

$$R(z) = \frac{e^{\Delta G(z)/RT}}{D(z)} \tag{5.15}$$

We can apply Eq.(5.15) directly to obtain $R(z)$ since we used the same slices along the bilayer normal when calculating both the $D(z)$ and $\Delta G(z)$ profiles, no interpolation is necessary. The error bars were calculated using the standard deviation of the independent simulations.

In figures 5.5 to 5.7 we present the resistance to permeation profiles $R(z)$ for the three different lipid structures, HT_4, $H_3(T_4)_2$, and $H_3(T_6)_2$, respectively. In order to make a comparison with atomistic simulations, we have denoted the regions of the membrane as described in chapter 3. For all three membranes, the hydrophobic core offers the greatest barrier to penetrating molecules. Notice how the resistance to permeation peaks in region 3 for all three membranes. The interphase where the head density is highest offers very little resistance compared with the center of the bilayer. The large error bars are a direct consequence of the error bars on the $\Delta G(z)$ profiles obtained from the CP method. This is because of the exponential dependence of $R(z)$ on $\Delta G(z)$. Similar errors are reported in Ref. [32]. Despite the large error bars just the respective maximums were different from sample to sample, the same overall trend was observed in each simulation.

The $R(z)$ profile obtained from the $H_3(T_6)_2$ bilayer was the only bilayer to have a similar shape to the resistance profiles found by atomistic simulations. The shorter tailed lipids failed to produce the "dip" of region 4. As we will discuss in the next section, the short tailed lipids do give a fare approximation of the overall permeability. Comparing our results with reference [32], we find that $H_3(T_6)_2$ bilayers $R(z)$ profile has a very similar shapes. The authors of this work (as well as those of Ref. [35]), used the *CHARMM* (Chemistry at **HAR**vard Molecular Mechanics, see ref. [55]) force field, which has full atomistic resolution. The peak of our $R(z)$ profile in "real" units comes to $\sim 1300 \times 10^6 s/cm^2$ whereas Ref. [32] report a peak value of $\sim 500 \times 10^6 s/cm^2$. By recalling that σ, m and ϵ can be interpreted as representing 2 water particles, our value is reduced to $650 s/cm^2$, comparable to to the atomistic value. We do not find as good agreement with the results presented in ref. [27] who report a peak value of $\sim 70 \times 10^6 s/cm^2$, but the general shape is very similar.

The agreement with atomistic simulations is quite remarkable. It implies that our simple model captures the same essential characteristics of the resistance that a membrane offers to a permeating water molecule. As explained in chapter 2, the main barrier of the membrane is the diffusion through the dense ordered regions of the tails, and the electrostatic barrier resulting from the transition from a medium with a

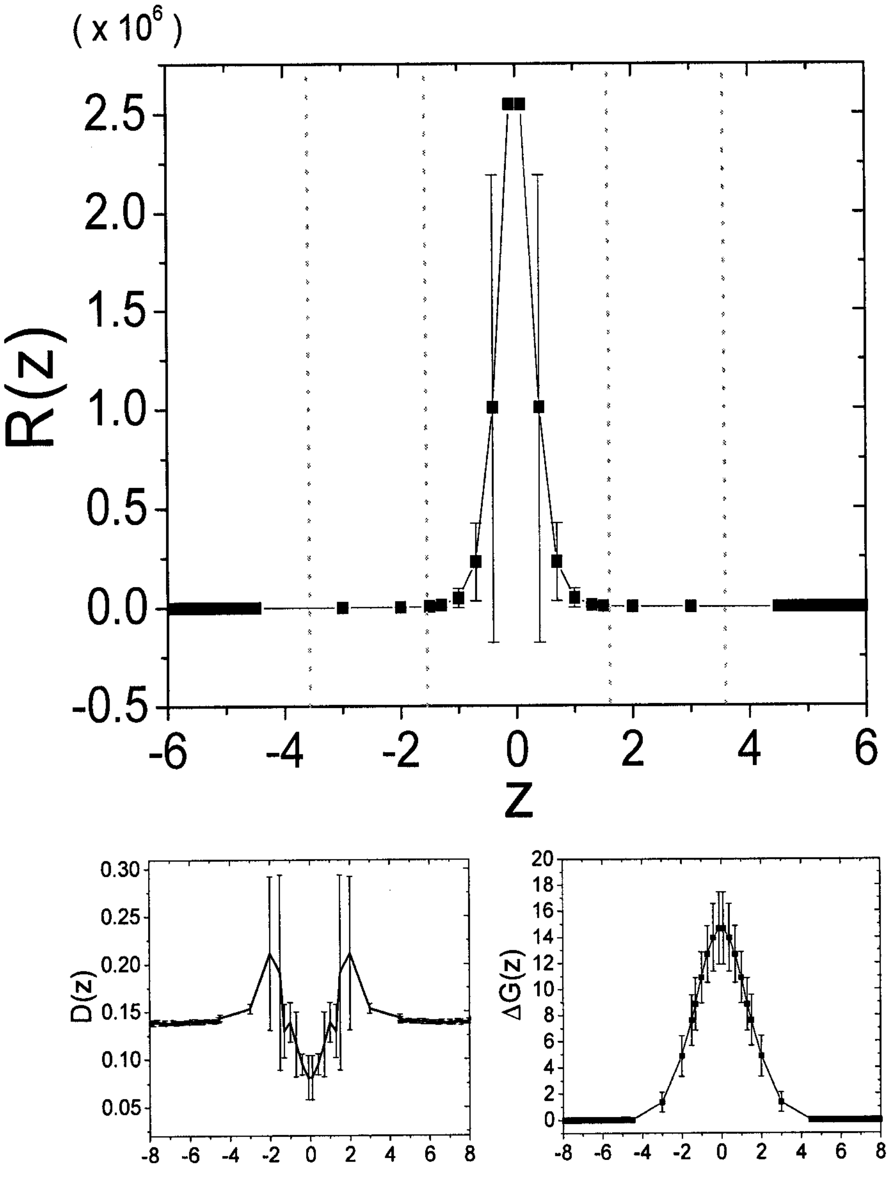

Figure 5.5: Permeation resistance for the TH_4 bilayer

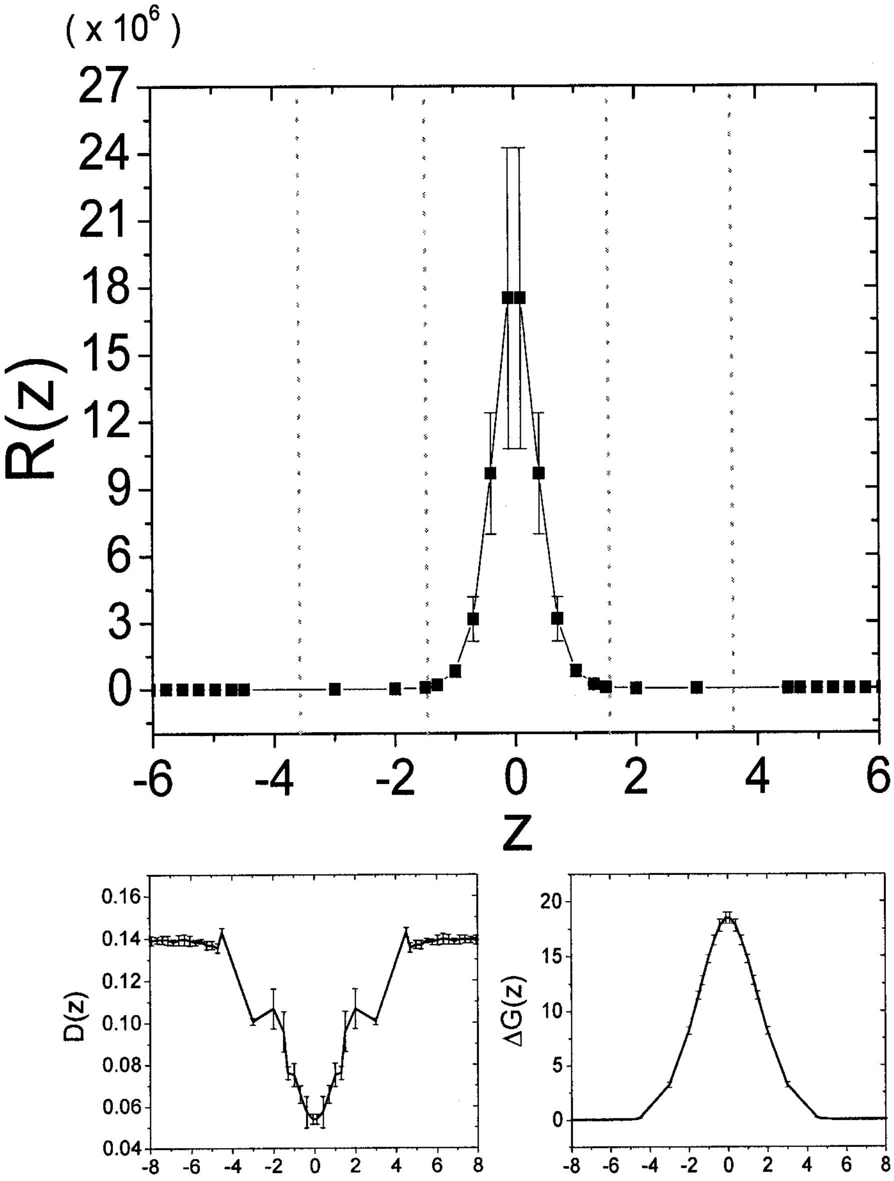

Figure 5.6: Permeation resistance for the $T_3(H_4)_2$ bilayer

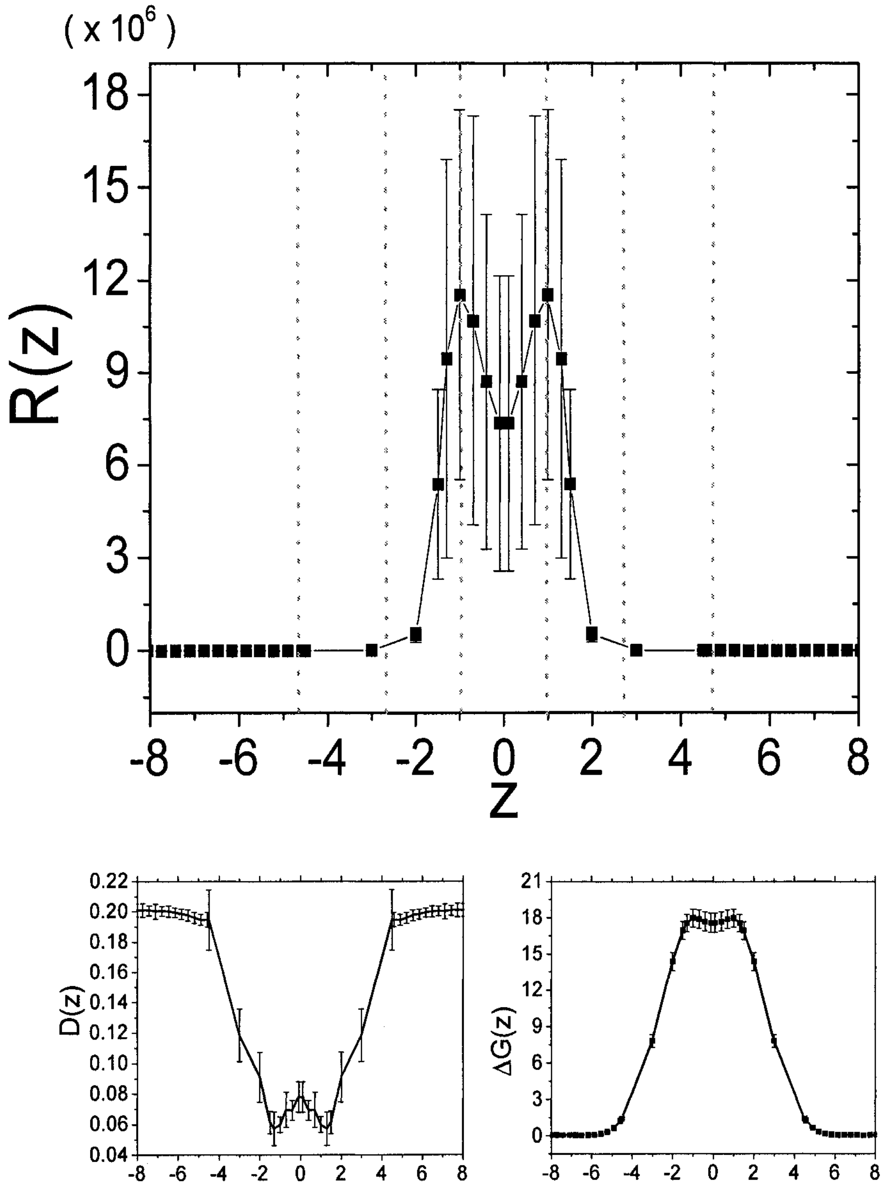

Figure 5.7: Permeation resistance for the $T_3(H_6)_2$ bilayer

high dielectric constant to one with a low dielectric constant. It is clear from fig. 5.7 that $D(z)$ has a minimum in region 3, the high density region of the membrane. Note too that $G(z)$ has a maximum in this region, therefore the electrostatic hindrance is well simulated by softcore potential.

5.3.2 Overall Permeability

Taking the integral of the resistance to permeation across the membrane we obtain the overall permeability. In figure 5.8 we compare the permeability values from our model to those obtained experimentally. In the chosen units, the $H_3(T_4)_2$ represents a lipid of $12C$ to $16C$ long chain (C = a CH_3 monomers) whereas the $H_3(T_6)_2$ lipids would have a chain length between $18C$ and $24C$ long. The experimental data shown are within this upper limit of these estimates. Our simulated lipids did not produce the same order of magnitude change in permeability as a function of length seen in the experimental data, although a small difference is observed.

The two tailed lipid have a permeability about an order of magnitude lower than the single chain architecture. The $\Delta G(z)$ barrier was much lower for the HT_4 lipid membranes therefore producing a much lower value of the permeability. The decrease in free energy may be a consequence of an increase in entropy in the case of the single tailed lipids. Some configurations available to the single tail lipids may not be accessible to double tailed lipids due to the attachment of the two tails. Therefore, a single tailed bilayer would more easily rearrange the tails to accommodate a permeating water molecule.

The calculated permeability for the $H_3(T_6)_2$ membrane is on the same order of magnitude as the experimental values. Assuming that the W beads represent 2 water molecules would give us even better agreement. Atomistic simulation have approximately the same precision, obtaining "order of magnitude" agreement.

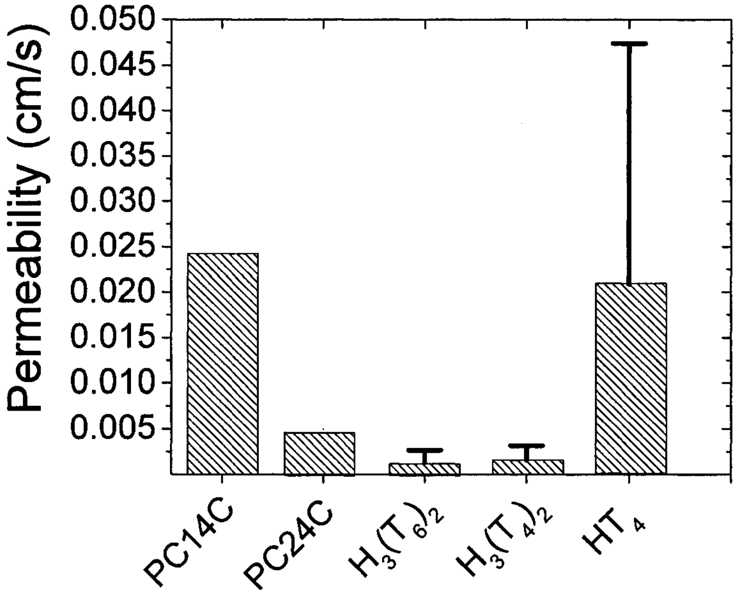

Figure 5.8: A comparison of the overall permeability of bilayers for each lipid geometry. The experimental data is presented in table 2.1. In calculating the water permeability for the simulated membranes, it was assumed that a bead represents 1 water molecule.

Chapter 6 Stretching, Membrane Structure and Permeability

In this chapter we look at the effects of stretching on the permeability of water through a bilayer membrane. We present results on the changes in structural properties as well as the diffusion, free energy and permeation resistance profiles across the membrane as the area per lipid is increased. Using the $R(z)$ profile we obtain the overall permeability for each of the stretched membranes. For most of this chapter, we examine the $H_3(T_6)_2$ lipid bilayers since we showed in the previous chapter that it most closely resembled membranes simulated with atomistic models. The simpler HT_4 lipids are used to study the effect of chain packing on the permeability of the membrane as it is stretched.

The results presented in this chapter took a substantial computational effort. Using the ISDM it took 340 CPU hrs to obtain the permeability of a $H_3(T_6)_2$ bilayer at a given stretch $\Delta a/a_0$. A large number of membranes were generated to obtain results of P as a function of $\Delta a/a_0$ which took on the order of 10^5 CPU hrs to obtain. This is an enormous computational task, which would have taken in the order of 10 years to perform on a single computer. To avoid the long waiting time, the simulations were performed using an "embarrassingly parallel" scheme on a Beowulf Cluster at Simon Fraser University. Independent samples were initialized and data obtained on separate CPU's thereby reducing the waiting time by a factor equal to the number of CPU's used at a time.

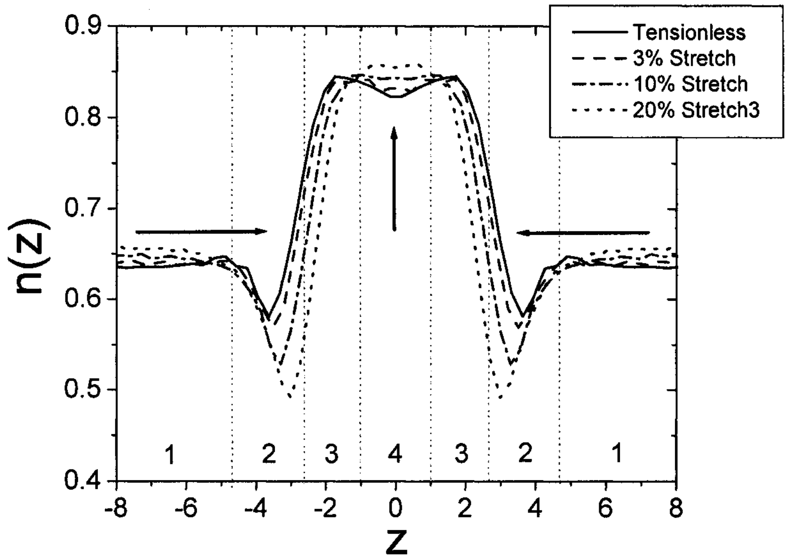

Figure 6.1: Effects of stretching on the total particle density across the membrane. The four regions model for the tensionless state is shown. Arrows highlight the effect of stretching on the profile.

6.1 Structural Changes with Stretching

6.1.1 Density and Membrane Thickness

In Chapter 4, we presented the effects of stretching on the stress profile of the membrane. It was observed that the stress was mainly located at the boundary where the lipid tails and water meet and the lipid heads are concentrated. At the center of the membrane, there was a region of zero stress, which corresponds well with region four of the membrane. In figure 6.1.1 we show the total density profiles for 4 different membrane extensions. As the membrane is stretched, we observe that the total density in region two decreases quite substantially while the density in region three remains nearly unaffected. The dip in density in region four is almost nonexistent at larger stretch values. In fact, the density in region four becomes the highest in the system.

Similar behaviour was found in the electron density profiles of the atomistic models of Feller et al. [38, 56] performed in a $NAPT$ ensemble, that is the number of

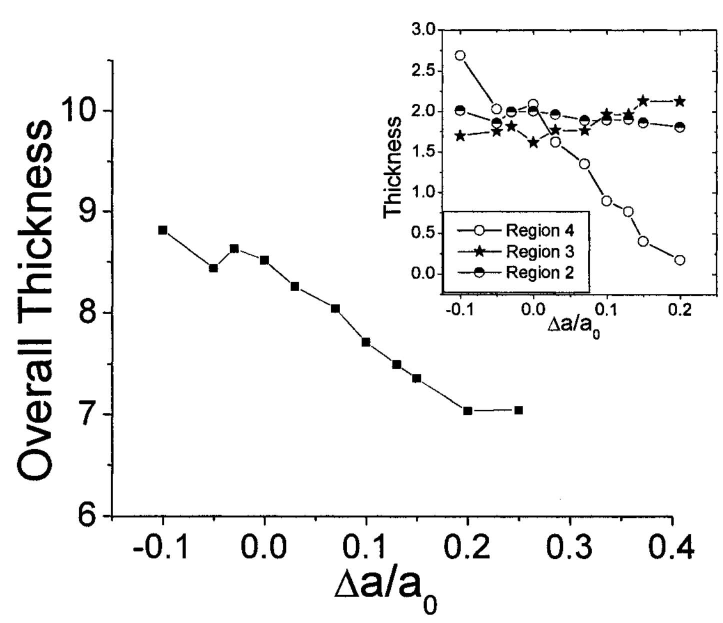

Figure 6.2: Decrease in the membrane thickness as a function of membrane expansion. Inset is the decrease in the thickness of each region as a function of stretch (see text).

particle N, the area A, the pressure P and the temperature T are held constant. In this extended NPT ensemble, the area of the plane containing the bilayer is forced to stay constant while the length along the bilayer normal varies so as to maintain the pressure constant. Little change was found in region three whereas the "dip" of region four was also found to increase and disappear. Their model did not show an increased void in region two.

Observing figure 6.2, we can see that the thickness and area of the membrane are linearly related. The thickness of the membrane is determined by the distance between the maximums of the head particle distributions. This result has been reported in experiments on membranes under small tension [57] and in atomistic simulations [38]. As we showed in chapter 4, we expect the membrane to thin as it is stretched in order to preserve the total volume. According to 6.1, we should observe that $\Delta a/a_0 = -\Delta d_t/d_0$. Plotting the thickness as a function of the area per lipid (as opposed to the relative expansion) we obtained a slope of -1.60 ± 0.05 which is somewhat smaller than the ratio $d_{t0}/a_0 = 2.0 \pm 0.1$ obtained using the values of table

4.2. This suggests that the membrane is compressing in an inhomogeneous way.

To get a good understanding of how the membrane was compressing, we divided each density profile in terms of the four region model. The $R1 - R2$ boundary (the boundary between regions 1 and 2) was defined as the intersection between the water density profile and the H density profile. The $R2 - R3$ boundary was defined as the location where the H particle density dips bellow 1 percent of the peak value. The $R3 - R4$ boundary was somewhat ambiguous. Region 4 represents the membrane interior, therefore it should offer a barrier to an escaping particle. From the $-d\Delta G/dz$ profile, we get the force exerted by the membrane on a water particle across the membrane. In the membrane interior, the force will either be 0, or be directed towards the center of the bilayer. Overlapping this profile, overtop the density allows us to get a good approximation of the location of the $R3 - R4$ boundary.

The inset of figure 6.2 shows that the region 4 undergoes the most significant compression while regions 3 and 2 remain at about the same thickness. A least square fit of the $R4$ thickness as a function of the area has a slope of -1.97 ± 0.14, in perfect agreement for an isochoric area expansion. This shows that the membrane interior only behaves as an incompressible fluid. The thickness in regions 2 and 3 stays near constant throughout the stretching process, therefore preserving the $W-T$ interphase.

6.1.2 Tail Ordering

Given that the membrane thins as the area per lipid increases, the next question to ask is how the lipid tails rearrange themselves. One way this can be done is by changing the amount of volume each lipid occupies. A (very) rough estimation of the amount of volume per lipid is obtained by assuming that each lipid is confined to a rectangle. Then, the volume per lipid is given by the total membrane area times the membrane thickness divided by the number lipids. As shown in the inset of figure 6.3, the volume per lipid stays virtually constant over a range of stretching. Therefore

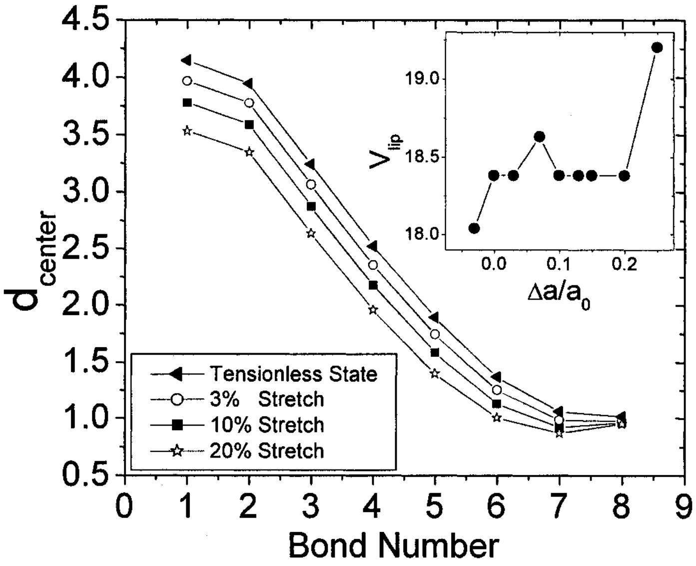

Figure 6.3: Stretching effects of the position of the different bonds between lipid beads. The position is given as the distance between the bond and the center of the bilayer, d_{center}. Inset is the volume per lipid as a function of stretch.

the lipids must rearrange in order to cope with the increased area. To examine this question further, we calculated the order parameter for the chains. Recall Eq.(2.6):

$$S_{CD} = \frac{1}{2}\left(3cos^2(<\theta>) - 1\right)$$

Ordered segments will have values close to -0.5 when perpendicular to the bilayer normal and 1 when parallel to the bilayer normal. Unordered bonds will have $S_{CD} \sim 0$. We distinguish each bond by labeling them with a number. The head of the lipid is composed of three particles connected by two bonds, 1 and 2. The tail bonds are labeled going down the lipid where 3 corresponds to the head-tail bonds and labels 4 to 8 correspond to the remaining tail segments. We averaged the S_{CD} values for each tail. The distance of each bond to the center of the membrane, d_{center}, was also obtained from simulation and the resulting profile is shown in fig. 6.3. The first five bonds move by about the same distance when the membrane is stretched in agrement with the observations made in the previous section. With increasing area

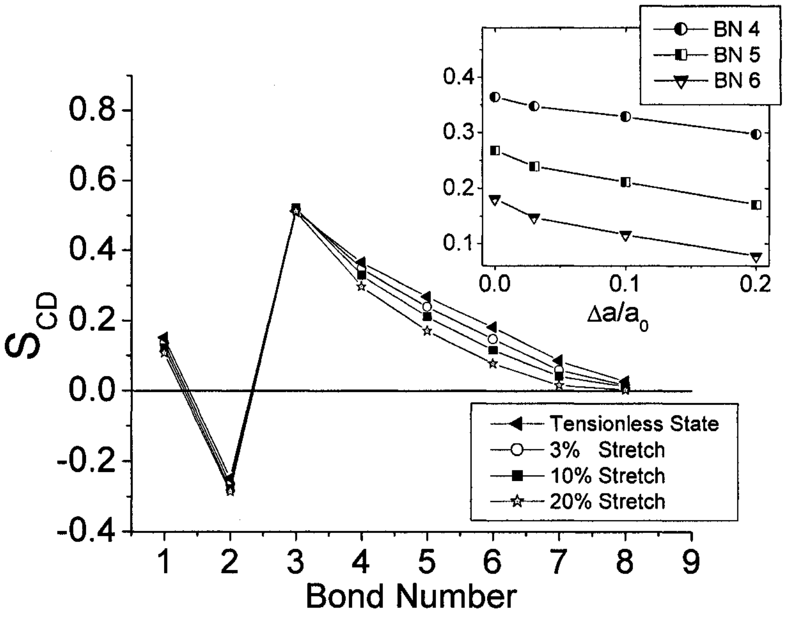

Figure 6.4: The stretching effects on the ordering of the lipid bonds. The inset shows the decrease in S_{CD} as a function of the area expansion for bonds in the dense region of the membrane.

per lipid, the tail beads are progressively forced down together into Region 4. In fact, for higher stretch values, we see that bond 8 is on average a bit higher than bond 7. This implies that some lipids may fold back on themselves.

Figure 6.4 shows that the ordering of the tails decreases with increasing area per lipid. Note how there is little change in S_{CD} for the higher bond indices. This lack of reorganization near the interphase could explain the decrease in density discussed earlier. The bonds that see the most change are the ones that correspond to region 3. Stretching reduces the ordering of the lipids in this region. In region 4, we can clearly see that the ordering is little affected by the stretching. In Ref. [38], the authors report a similar decrease in ordering in the high density region of the tails. They also report significant differences in the ordering of the lipid head section whereas we do not.

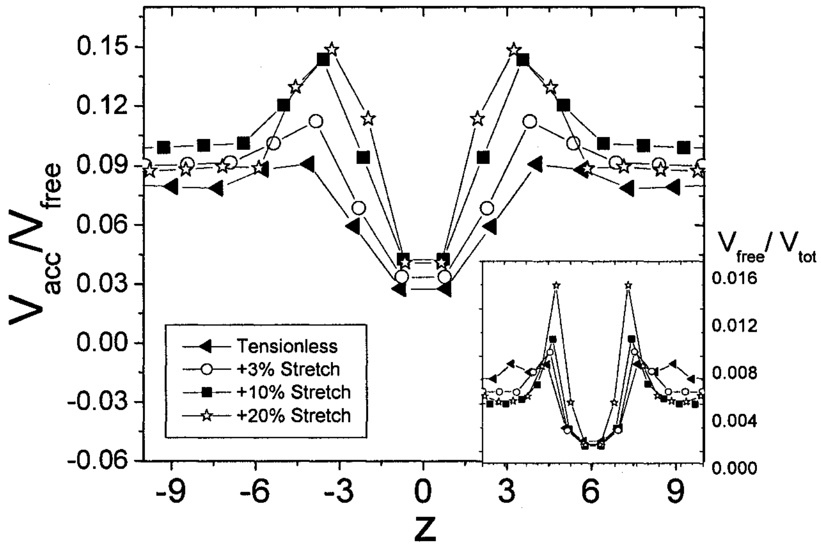

Figure 6.5: Accessible free volume to free volume ratio profile for a particle size $r^* = 0.1$ for the $T_3(H_6)_2$ BLM at different stretch. In the inset is the free volume to total volume profile.

6.1.3 Free Volume and Hole Distribution

Another quantity which is of interest is the free volume distribution in the membrane. To understand the decrease in order in region 3 of the membrane, we looked at the distribution of free volume in the bilayer for different stretches. The free volume was defined as any space outside a distance of σ_{LJ} from any particle in the system [58]. To obtain it from simulation, we divide the system along the x, y and z directions creating a $3D$ grid of voxels. By excluding all voxels less than σ_{LJ} away from the particles in the system, we are left with a set of voxels which is the free volume in the system. For the analysis presented here, we used a $75 \times 75 \times 100$ grid. We experimented with a few grid sizes, but found little difference in the final distribution of free volume. To get an idea of the space available to a particle of radius r^*, we calculated the accessible free volume, defined as any free volume element which is more than $\sigma + r^*$ away from all system particles [58].

We performed an analysis of the distribution of both free volume and accessible free volume for "test" particles of three different sizes, $r = 0.1, 0.25, 0.5$. In figure 6.5, we present the ratio of the accessible free volume V_{acc} to the total free volume V_{free} for a "test" particle of size $r^* = 0.1$. Also shown is the ratio of the total free volume to the total volume as a function of the position in the cell. Not surprisingly, we observe a peak in the free volume at the interface where the head sections dominate. This is the same region where we observed a dip in the overall density. This is also where V_{acc}/V_{free} exhibits the most substantial changes with stretch. Stretching the membrane also seems to increase the ratio of free volume inside the membrane in regions three and four. This is most likely a result of the decreased order in the tail sections since the density does not vary substantially (in fact increases!) in this area.

The most surprising result here is the small percentage of free volume that is actually available even to a particle of radius 0.1. This suggests that the free volume is scattered in very small pockets instead of a single large globule, in which case V_{acc}/V_{free} would be much closer to one. At the center of the bilayer, we see an increase in the accessible free volume with increased membrane stretch. The profiles discussed here differ considerably from those obtained from atomist models Ref. [58, 33]. The studies using atomistic models predict much higher free volume to volume ratios. We obtained ratios an order of magnitude smaller because of the large radius assumed for the size of a water water molecule. In Ref. [33] they assumed σ was half the interaction radius of a single, "atomically correct", water molecule whereas we assumed it to be σ for a W bead, roughly four times larger.

To get an idea of how the free volume is scattered within the membrane, we studied the distribution of accessible hole size. This analysis is similar to the study done by Marrink, Sok and Berendsen [58]. A hole is defined as a cluster of connected free volume voxels. A routine was written that systematically identified the connected neighbors for each of the free volume voxel. We first started from a voxel at a corner of the simulation box and tagged it with an integer N_i. We then checked the neighboring sites to verify if any of them were free volume sites. If so, we tagged them with the same integer, N_i. If this voxel had been previously tagged with an integer N_{i-k}, we look through the previously tagged voxels and change each N_{i-k} tag

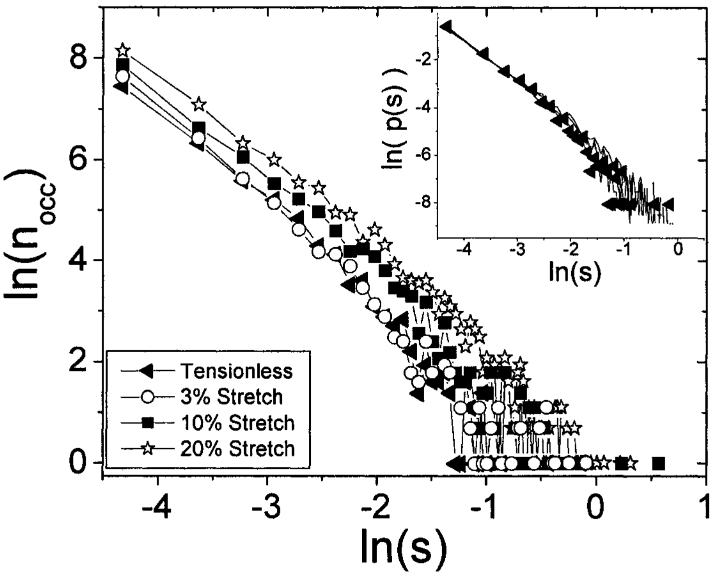

Figure 6.6: Accessible hole size distribution, $n_{occ}(s)$ for a "test" particles of radius $r^* = 0.1$ for region 3 of the membrane at different stretch. Inset is the probability distribution, $p(s)$ of the hole sizes s for region three at different stretch. The triangle denote the tensionless state whereas straight lines were used for the other 3 stretch values.

to N_i. Repeating this procedure for all the voxels, while paying special attention to the periodic boundary conditions, we create a map of tagged voxels. The clusters in this map will all have the same integer. Using this procedure for the accessible free volume we obtain the accessible free volume clusters. To get an idea of where the clusters are situated in the system, we calculated the "center of mass" of each cluster and classified them according to the four region model of the bilayer.

Shown in figure 6.6 are the resulting accessible cluster size distributions, n_{occ} for a "test" particle of size $r^* = 0.1$ in region three. This is the most important region for the permeation process so we restrict our analysis to this part of the membrane. The overall number of clusters increases with increasing stretch. This is expected since we saw that the accessible free volume increases with stretching. There also seems to be two regimes for the membranes near the tensionless state, whereas just one regime for the higher stretch values. The data is somewhat noisy for the larger cluster sizes, so no solid conclusion can be drawn.

Normalizing the cluster size distribution by the total number of clusters found at a particular stretch gives the cluster size probability distribution, $p(s)$. The $p(s)$ is presented in the inset of figure 6.6. The two regimes are once again apparent. For the small cluster sizes the probability shows no dependence on stretch whereas for larger cluster sizes, we see a different slope for each stretch. This implies that stretching produces a slightly higher probability to find larger clusters in region three and therefore should lead to a higher diffusion in this region for small molecules.

All the distributions show a power law behaviour for every stretch values. The authors of Ref. [58] also observed a scaling law behaviour and explain it's emmergence using percolation theory. The free volume of a system is said to percolate when it connects the boundaries [58]. Percolation theory predicts that the free volume in the system should scale according to a power law of the form $s^{-\tau}$ when clusters are small and scattered, which is just what we observe. A quantitative analysis of the data is beyond the scope of such a preliminary study and we refer the reader to Ref. [58] for additional information. Analysis of the accessible free volume for $r^* \geq 0.1$ cluster distributions led to similar results, but with a much larger error.

6.2 Diffusion, Free Energy and Resistance to Permeation

6.2.1 Diffusion and Free Energy Profiles

Given the structural changes which occur with increased area per lipid, we expect that both the diffusion and free energy profiles show changes as the membrane is stretched. In figure 6.7 we present the diffusion profile and free energy profiles in the tensionless state, as well as at 10% and 20% stretch. The diffusion profile is considerably affected by the increased area per lipid. The interphase becomes much sharper and the diffusion at the center of the membrane is much more homogeneous. The minimum of the profile, which occurs in region three, increases and the peak in region four is reduced. This is consistent with the changes observed in the structural properties. As the membrane is stretched, the membrane interior thins and the

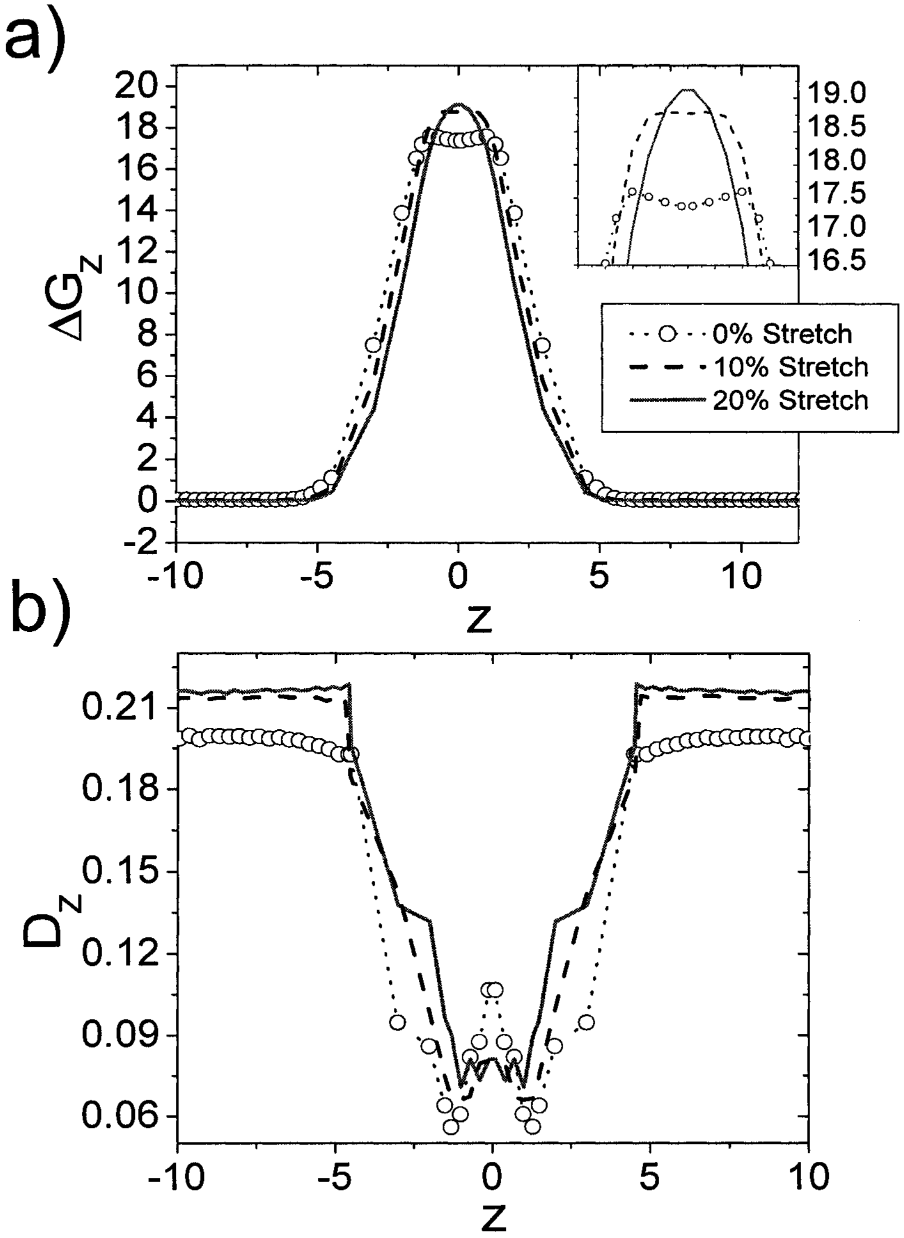

Figure 6.7: a) Stretching effects on the free energy profiles. Inset shows the top of the profile. b) Stretching effects on the diffusion profile.

tail ordering decreases. The density at the center of the membrane also becomes more homogeneous and therefore, we should expect that the diffusion coefficient also becomes more homogeneous across region three and four. The rise in diffusion observed in region three is most likely due to the increase in free volume found in this part of the membrane.

Changes to the free energy profile as a function of membrane stretch are less considerable. As the thickness of the tail section of the membrane decrease the base of the free energy profile thins. We also observe an increase in the value of free energy in region 4 as this region of the membrane is thins. The changes in free energy profile are mainly due to the changes in the density inside the membrane. This is most apparent in region 4. Both the free energy and diffusion profiles of the membrane at 20 percent extension resemble the profiles for the short tailed $H_3(T_4)_2$ lipid bilayer, which is in agreement with our model that region four reduces with membrane extension.

6.2.2 The Resistance to Permeation

The resistance to permeation is considerably affected by stretching. The most significant effect is the increase at the center of the membrane. Stretching causes the "base width" of the profile to thin, while the $R(z)$ values in region 4 increase as indicated by the arrows in figure 6.8. This is not surprising since region 4 was the only part of the membrane which thinned with stretching. The absolute values of the resistance at the center of the membrane was found to increase by about a factor of 4 as a result of the change in $\Delta G(z)$. From the profile data 6.7, we find that the change in $\Delta G(z)$ at the center of the membrane between 0% and 20% stretch was 1.5 implying $R(z') \sim e^{1.5} \sim 4.5$ slightly larger than the increase observed. The diffusion in this region was found to decrease but only by a factor of about 1.5, thus affecting the value of $R(z)$ much less than $\Delta G(z)$.

Although there seems to be a significant increase of $R(z)$ with stretching, we point out here that the error bars are about large as the value itself. In fact, we